

# Protostellar Disk Formation Enabled by Removal of Small Dust Grains

Bo Zhao<sup>1\*</sup>†, Paola Caselli<sup>1</sup>, Zhi-Yun Li<sup>2</sup>, Ruben Krasnopolsky<sup>3</sup>, Hsien Shang<sup>3</sup>,  
Fumitaka Nakamura<sup>4</sup>

<sup>1</sup>Max-Planck-Institut für extraterrestrische Physik (MPE), Garching, Germany

<sup>2</sup>University of Virginia, Astronomy Department, Charlottesville, USA

<sup>3</sup>Academia Sinica Institute of Astronomy and Astrophysics, Taipei, Taiwan

<sup>4</sup>National Astronomical Observatory of Japan, Tokyo, Japan

9 February 2016

## ABSTRACT

It has been shown that a realistic level of magnetization of dense molecular cloud cores can suppress the formation of a rotationally supported disk (RSD) through catastrophic magnetic braking in the axisymmetric ideal MHD limit. In this study, we present conditions for the formation of RSDs through non-ideal MHD effects computed self-consistently from an equilibrium chemical network. We find that removing from the standard MRN distribution the large population of very small grains (VSGs) of  $\sim 10$  Å to few 100 Å that dominate the coupling of the bulk neutral matter to the magnetic field increases the ambipolar diffusivity by  $\sim 1$ – $2$  orders of magnitude at densities below  $10^{10}$  cm<sup>-3</sup>. The enhanced ambipolar diffusion (AD) in the envelope reduces the amount of magnetic flux dragged by the collapse into the circumstellar disk-forming region. Therefore, magnetic braking is weakened and more angular momentum can be retained. With continuous high angular momentum inflow, RSDs of tens of AU are able to form, survive, and even grow in size, depending on other parameters including cosmic-ray ionization rate, magnetic field strength, and rotation speed. Some disks become self-gravitating and evolve into rings in our 2D (axisymmetric) simulations, which have the potential to fragment into (close) multiple systems in 3D. We conclude that disk formation in magnetized cores is highly sensitive to chemistry, especially to grain sizes. A moderate grain coagulation/growth to remove the large population of VSGs, either in the prestellar phase or during free-fall collapse, can greatly promote AD and help formation of tens of AU RSDs.

**Key words:** disk formation, ambipolar diffusion, dust grain size, cosmic-ray ionization

## 1 INTRODUCTION

The formation of rotationally supported disk (RSD) from magnetized dense molecular cloud cores is a long-standing problem in star formation. Although RSDs are frequently observed around young stellar objects (Williams & Cieza 2011), including deeply embedded sources (Tobin et al. 2012, 2013), theoretical studies have found it difficult to form such disks due to strong magnetic braking which catastrophically removes most angular momentum of circumstellar gas. This is the so-called “magnetic braking catastrophe” in disk formation (Mestel & Spitzer 1956; Allen et al. 2003; Mellon & Li 2008; Li et al. 2011).

In the axisymmetric ideal MHD limit, the magnetic field strength required for such catastrophic magnetic braking is moderate (Allen et al. 2003). The observed magnetization of dense cores,

quantified by the dimensionless mass-to-flux ratio  $\lambda$ , has a typical value of  $\lambda \sim 2$ – $3$  from OH Zeeman survey (Troland & Crutcher 2008). Although uncertainty exists due to OH depletion at high densities (Tassis et al. 2014), the bulk of dense core should still have  $\lambda \sim$  a few. Such a strong magnetic field, if not sufficiently decoupled from collapsing matter, can transport most angular momentum away from the circumstellar region via magnetic braking, and hence suppress the formation of RSDs (Mellon & Li 2008; Hennebelle & Fromang 2008).

In reality, dense cores are only slightly ionized (Bergin & Tafalla 2007), and magnetic fields are expected to at least partially decouple from neutral matter through non-ideal MHD effects, including ambipolar diffusion (AD), Ohmic dissipation, and Hall effect (e.g., Nakano et al. 2002). Their effects on disk formation have been studied previously (Mellon & Li 2009; Dapp & Basu 2010; Li et al. 2011; Krasnopolsky et al. 2011; Dapp et al. 2012; Tomida et al. 2013, 2015; Tsukamoto et al. 2015a,b; Masson et al. 2015;

\* Contact e-mail: bo.zhao@mpe.mpg.de

† Present address: Giessenbachstr. 1, D-85748, Garching, Germany

Wurst et al. 2015); however, whether a large (say 50 AU sized), long-lived RSD can form or not remains unclear. Most of these studies show that AD and Ohmic dissipation can only help to form a small RSD ( $<10$  AU) early in the first core phase (Larson 1969); but whether such disk can survive or grow in the subsequent evolution is unclear due to numerical difficulties. The RSD formed via Hall effect can indeed be larger ( $\sim 30$  AU), yet only when the direction of magnetic field is nearly anti-parallel to the net rotation axis of dense core (Krasnopolsky et al. 2011; Braiding & Wardle 2012; Tsukamoto et al. 2015b; Wurst et al. 2015). In a realistic turbulent core, it is unclear whether such a requirement in field geometry can be satisfied throughout the entire protostellar evolution phase. Therefore, the inconsistency between disks formed in theoretical calculations and those observed around young stellar objects remains unresolved. Shu et al. (2006) and Krasnopolsky et al. (2010) suggest that in order to bridge this gap, magnetic diffusivity over a large circumstellar region must be at least 1 order of magnitude above the classical value used in most studies.

The magnetic diffusivity due to non-ideal MHD effects is essentially determined by chemistry and microscopic physical processes (Oppenheimer & Dalgarno 1974; Umebayashi & Nakano 1990; Nakano et al. 2002). The key is to calculate the fractional abundances of charged species (electron, ions, and charged grains) and their effective conductivities. However, uncertainty still exists in such calculations due to the lack of observational constraints on grain size distribution in dense molecular cloud cores (e.g., Kim et al. 1994). Typical chemistry models either choose a single grain size (e.g., Umebayashi & Nakano 1990), or adopt the standard MRN (Mathis-Rumpl-Nordsieck; Mathis et al. 1977) size distribution from diffuse interstellar clouds (e.g., Nakano et al. 2002). However, the choice of grain size can greatly affect the ionization fraction (Nishi et al. 1991) and the magnetic diffusivity (Dapp et al. 2012); because grains not only provide surface for recombination of ions and electrons, but also couple to the magnetic field if they are charged (the smaller the grain, the stronger the coupling). Therefore, non-ideal MHD studies on disk formation should pay special attention to the effect of grain size on magnetic diffusivities.

Recent studies have shown evidence of magnetic diffusivity enhancement by removing very small grains. Wardle & Ng (1999) find that removal of  $\sim 10^2$  Å grains greatly reduces the Hall conductivity and hence increases the diffusivity for Hall effect; however, its impact on ambipolar diffusivity has not been addressed. Dapp et al. (2012) explore different single sized grains ranging from  $\sim 0.01$ – $0.1$   $\mu\text{m}$ , and reveal that the effective magnetic diffusivity (including both Ohmic dissipation and AD) with  $\sim 0.1$   $\mu\text{m}$  grains is 1–2 orders of magnitude higher than that with a MRN size distribution (see their Fig.2). However, they did not elaborate on how this affects disk formation. Padovani et al. (2014) apply post-processing chemistry models to the ideal MHD simulations of Joos et al. (2012), and find that the size of matter-field decoupling region increases significantly with a “truncated” MRN distribution ( $a_{\text{min}} = 0.1$   $\mu\text{m}$ ) compared with the full MRN distribution. To verify their findings, a more complete chemical network and a self-consistent calculation are necessary. Inspired by the seminal work of Padovani et al. (2014), we improve their chemical network and revisit the non-ideal MHD effects on disk formation in this paper, with a particular focus on enhancing AD by truncating very small grains (VSGs:  $\sim 10$  Å to few 100 Å) off the MRN distribution. The truncation is a simple representation of the actual removal of very small grains in dense cores of molecular clouds.

There is observational evidence for the removal of very small

grains in dense cores. Extinction (optical and near-infrared) and polarimetric observations of dense molecular clouds indicate that dust grains have larger sizes than those in diffuse interstellar medium (Cardelli et al. 1989; Vrba et al. 1993). Recent discovery of “core-shine” (light scattered by large dust grain up to 1  $\mu\text{m}$ ; Pagani et al. 2010; Steinacker et al. 2010) from nearby dense cores also implies that grains have grown substantially to larger sizes. Evidence of grain growth has also been collected using multi-wavelength studies (Schnee et al. 2014; Forbrich et al. 2015). Two grain growth mechanisms can operate in such cold dense environment: accretion onto grain mantles (e.g., Tielens & Hagen 1982; Hasegawa et al. 1992) and grain coagulation (e.g., Chokshi et al. 1993; Dominik & Tielens 1997). The latter — grain coagulation — has been shown theoretically to be rather efficient in removing small grains ( $<0.1$   $\mu\text{m}$ ) from the MRN size distribution within a few  $10^6$  years (Rossi et al. 1991; Ossenkopf 1993; Ormel et al. 2009; Hirashita 2012). Such a process may have already finished during the quiescent, slowly-evolving prestellar phase if the cloud is magnetically supported (Shu et al. 1987; Mouschovias & Ciolek 1999). Therefore, the exclusion of VSGs from MRN size distribution may in fact be more appropriate for evaluating the magnetic diffusivity in dense cores.

The rest of the paper is organized as follows. Section 2 describes the chemistry model we adopted in our analytical and numerical calculations. The initial conditions of the simulation set are listed in Section 3, together with an overview of the results. In Section 4, we first demonstrate the cause of AD enhancement by eliminating VSGs, using simple analytical results from our chemistry model. The simulation results are then presented in Section 5, with a comprehensive interpretation of the effects of various parameters on the formation of different types of RSDs. We summarize the main results and put them in context in Section 6.

## 2 CHEMISTRY MODEL

Magnetic diffusivities are determined by chemistry and microscopic physical processes, i.e., the degree of ionization and the thermal collision between different species. The ionization fraction of charged species can be obtained from standard chemistry models (Oppenheimer & Dalgarno 1974; Umebayashi & Nakano 1990). To self-consistently couple the chemistry with MHD simulations during run-time, we adopt a simple equilibrium network based on Padovani et al. (2014), which is described as below.

### 2.1 Ionization Rate

The dominant source of ionization in dense molecular cloud cores is cosmic-rays. The interstellar UV-radiation becomes less important due to the relatively high column density in dense cores (visual extinction  $A_V > 4$  mag, McKee 1989). The cosmic-ray ionization rate  $\zeta_0^{\text{H}_2}$  at cloud core scale ranges from  $\sim 10^{-17}$   $\text{s}^{-1}$  to  $\sim 10^{-16}$   $\text{s}^{-1}$ , based on both theoretical models and observations (e.g., Spitzer & Tomasko 1968; Caselli et al. 1998; van der Tak & van Dishoeck 2000). The attenuation of cosmic-rays through energy loss of cosmic-ray particles can change the local ionization rate in dense cores. Umebayashi & Nakano (1981) have shown that the cosmic-ray ionization rate can be well described by the following relation:

$$\zeta^{\text{H}_2} = \zeta_0^{\text{H}_2} \exp(-\Sigma_{\text{H}_2}/\Sigma_0) \quad (1)$$

where  $\Sigma_0 = 96 \text{ g cm}^{-2}$  is the attenuation length, and the  $\text{H}_2$  column density  $\Sigma_{\text{H}_2}$  can be estimated from the gas density  $\rho$  as (Nakano et al. 2002):

$$\Sigma_{\text{H}_2} \approx \frac{4kT\rho}{\pi G\mu m_{\text{H}}} \quad (2)$$

where  $T$  is the gas temperature,  $\mu = 2.36$  is the mean molecular weight per hydrogen atom (assuming a mass fraction of 71% hydrogen, 27% helium, and 2% metals), and  $m_{\text{H}}$  is the mass of a hydrogen atom. With this relation, the exponential decrease in Eq. 1 only becomes important at number density  $n(\text{H}_2) \gtrsim 10^{11} \text{ cm}^{-3}$ .

Above a few  $10^{12} \text{ cm}^{-3}$ , the ionization rate due to cosmic-ray decreases abruptly below  $10^{-19} \text{ s}^{-1}$ . However, at such densities, the radioactive decay of long-lived  $^{40}\text{K}$  or short-lived  $^{26}\text{Al}$  becomes the dominant source of ionization. They contribute to  $\zeta^{\text{H}_2} (^{40}\text{K}) = 1.1 \times 10^{-22} \text{ s}^{-1}$  and  $\zeta^{\text{H}_2} (^{26}\text{Al}) = 7.3 \times 10^{-19} \text{ s}^{-1}$ , respectively, based on the newly measured abundances of radionuclides in primitive Solar nebula (Umebayashi & Nakano 2009; Cleaves et al. 2013). The short half-life 0.74 Myr of  $^{26}\text{Al}$  is still much longer than the time-scale of protostellar collapse phase in this study. Therefore, we place a lower limit to the ionization rate at  $7.3 \times 10^{-19} \text{ s}^{-1}$ .<sup>1</sup>

## 2.2 Chemical Network

The equilibrium chemical network used in this study is derived from Padovani et al. (2014, Appendix A), with additional grain species ( $g^+$  and  $g^0$ ), instead of assuming all grains are negatively charged. The simplified network includes neutral species  $\text{H}_2$ , heavy molecules (denoted collectively as “m”), and heavy metals (denoted collectively as “M”) and charged species  $e^-$ ,  $\text{H}^+$ ,  $\text{H}_3^+$ ,  $m^+$  (typically  $\text{HCO}^+$ ), and  $M^+$ , as well as neutral and singly charged dust grains  $g^0$ ,  $g^-$ , and  $g^+$ . The abundance of neutral molecules and metals are fixed at  $x(m) \approx 6 \times 10^{-4}$  and  $x(M) \approx 4 \times 10^{-8}$  (Caselli et al. 2002a; Padovani et al. 2014).

Because of the relatively unconstrained grain size distribution in dense molecular clouds, we choose the standard  $-3.5$  power law as in the MRN distribution (Mathis et al. 1977), but with a varying minimum grain size  $a_{\text{min}}$  (the maximum grain size  $a_{\text{max}}$  is fixed at  $0.25 \mu\text{m}$  for most models, although a higher value of  $1 \mu\text{m}$  is also considered in some cases). We also fix the total grain mass at  $q = 1\%$  of the gas mass. The density of grain material is taken to be  $\rho_g = 2.3 \text{ g cm}^{-3}$  (Kunz & Mouschovias 2009), i.e., the average density of silicates. Therefore, the size distribution function is given by,

$$\frac{dn(a)}{da} = Ca^{-3.5}, \quad (3)$$

where the normalization factor  $C$  can be determined as,

$$C = \frac{3qm_{\text{H}}}{4\pi\rho_g(\sqrt{a_{\text{max}}} - \sqrt{a_{\text{min}}})}n(\text{H}_2). \quad (4)$$

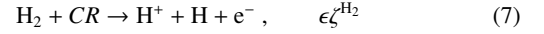
Therefore, the total number density of grains can be written as a function of the minimum grain size  $a_{\text{min}}$ ,

$$n(g) = \frac{3qm_{\text{H}}}{10\pi\rho_g(a_{\text{max}}^{0.5} - a_{\text{min}}^{0.5})}(a_{\text{min}}^{-2.5} - a_{\text{max}}^{-2.5}), \quad (5)$$

which depends strongly on  $a_{\text{min}}$ .

The abundances of all species are solved algebraically assuming a steady-state in ionization, where creation and destruction of

charged species balance each other (given the short time-scale of order a few  $10^1$  years for the processes involved, Caselli et al. 2002a). The cosmic-ray ionization of  $\text{H}_2$  is the primary source for  $\text{H}^+$  and  $\text{H}_3^+$  production in dense molecular clouds, which initiates the subsequent chemical reactions in the network through the relations:



in which  $\epsilon \approx 0.05$  (Shah & Gilbody 1982).  $\text{H}_2^+$  reacts immediately with  $\text{H}_2$  to form  $\text{H}_3^+$ , we thus consider  $\text{H}_3^+$  as a direct product of the ionization process given in Eq. 6.

The steady-state chemical equations are summarized below, with rate coefficients derived from Kunz & Mouschovias (2009). The charge transfer (CT) rate between atomic and molecular ions is  $\beta \approx 2.5 \times 10^{-9} \text{ cm}^3 \text{ s}^{-1}$ . The recombination rate of atomic ions and electrons is  $\alpha_{\text{rec}} \approx 2.8 \times 10^{-12} (300\text{K}/T)^{0.86} \text{ cm}^3 \text{ s}^{-1}$ . The dissociative recombination (DR) rate of electrons and molecular ions is  $\alpha_{\text{dr}} \approx 2.0 \times 10^{-7} (300\text{K}/T)^{0.75} \text{ cm}^3 \text{ s}^{-1}$ . The rate coefficients involving grains are calculated from Kunz & Mouschovias (2009, Appendix A, see also Draine & Sutin 1987) and averaged over the MRN size distribution (ranging from  $a_{\text{min}}$  to  $a_{\text{max}} = 0.25 \mu\text{m}$ ):

$$\langle \alpha_{\text{xg}} \rangle = \frac{\int_{a_{\text{min}}}^{a_{\text{max}}} \alpha_{\text{xg}} \frac{dn}{da} da}{\int_{a_{\text{min}}}^{a_{\text{max}}} \frac{dn}{da} da}, \quad (8)$$

where  $\alpha_{\text{xg}}$  represents the recombination rate between a charged species “x” and a grain species “g” (neutral grain  $g^0$ , or charged grains  $g^-$  and  $g^+$ ). For simplicity, we denote the averaged quantity  $\langle \alpha_{\text{xg}} \rangle$  as  $\alpha_{\text{xg}}$  hereafter.

The protons  $\text{H}^+$  produced by ionization of  $\text{H}_2$  are mainly destroyed by CT with molecules and recombination on grains:

$$\epsilon\zeta^{\text{H}_2}n(\text{H}_2) = [\beta n(m) + \alpha_{\text{ig}^-}n(g^-) + \alpha_{\text{ig}^0}n(g^0)]n(\text{H}^+). \quad (9)$$

The production of  $\text{H}_3^+$  by ionization of  $\text{H}_2$  is balanced by CT with heavy molecules, DR with electrons, and recombination on grains:

$$(1 - \epsilon)\zeta^{\text{H}_2}n(\text{H}_2) = [\beta n(m) + \alpha_{\text{dr}}n(e^-) + \alpha_{\text{ig}^-}n(g^-) + \alpha_{\text{ig}^0}n(g^0)]n(\text{H}_3^+). \quad (10)$$

Molecular ions  $m^+$  are mainly formed via CT of  $\text{H}_3^+$  with heavy molecules, and destroyed by CT with metals, DR with electrons, and recombination on grains:

$$\beta n(\text{H}_3^+)n(m) = [\beta n(M) + \alpha_{\text{dr}}n(e^-) + \alpha_{\text{ig}^-}n(g^-) + \alpha_{\text{ig}^0}n(g^0)]n(m^+). \quad (11)$$

Metal ions  $M^+$  are mainly formed via CT of  $\text{H}_3^+$  and  $m^+$  with metal atoms, and are destroyed by recombination with free electrons and on grains:<sup>2</sup>

$$\beta[n(\text{H}_3^+) + n(m^+)]n(M) = [\alpha_{\text{rec}}n(e^-) + \alpha_{\text{ig}^-}n(g^-) + \alpha_{\text{ig}^0}n(g^0)]n(M^+). \quad (12)$$

The ionization equilibrium equations for charged grains are given as follows. Grains are negatively charged mainly by sticking electrons on the surface of neutral grains (assuming sticking probability as 1.0), while neutralized by recombination with ion species

<sup>1</sup> As will be shown in § 4, the main effects of this study occur at densities below  $10^{10} \text{ cm}^{-3}$ , which are not affected by the limiting ionization rate.

<sup>2</sup> Even though the recombination rate  $\alpha_{\text{rec}}$  is  $\gtrsim 10^4$  smaller than  $\alpha_{\text{ig}^-}$ , the recombination between metal ions and electrons can become very important when  $n(g^-) \ll n(e^-)$  for large grain sizes.

and CT with positively charged grains. So the equilibrium equation for  $g^-$  is:

$$[\alpha_{\text{eg}^0} n(e^-)] n(g^0) = [\alpha_{\text{ig}^-} \sum n(i^+) + \alpha_{\text{g}^+ \text{g}^-} n(g^+)] n(g^-). \quad (13)$$

Positively charged grains are formed by sticking ion species on the surface of neutral grains (sticking without fail), and are neutralized by recombination with electrons and CT with negatively charged grains. So the equilibrium equation for  $g^+$  is:

$$[\alpha_{\text{ig}^0} \sum n(i^+)] n(g^0) = [\alpha_{\text{eg}^+} n(e^-) + \alpha_{\text{g}^+ \text{g}^-} n(g^-)] n(g^+), \quad (14)$$

where we denote ion species collectively as  $\sum n(i^+) = n(\text{H}^+) + n(\text{H}_3^+) + n(\text{m}^+) + n(\text{M}^+)$ . The CT between a charged grain and a neutral grain does not appear because it is already in steady-state and cancels out from both sides of the equation. Note that the grain-grain CT terms in right-hand side of Eq. 13 and Eq. 14 can be neglected in low density regimes (to simplify the solution) where the abundances of electrons and ions are orders of magnitude higher than that of grains, but not for higher densities when most electrons and ions have recombined and grains become the main charge carriers.

The set of steady-state equations Eq. 9-14 are closed by charge neutrality,

$$n(g^-) + n(e^-) = n(\text{H}^+) + n(\text{H}_3^+) + n(\text{m}^+) + n(\text{M}^+) + n(g^+), \quad (15)$$

and the constraint on the total number of grains,

$$n(g) = n(g^0) + n(g^-) + n(g^+). \quad (16)$$

The above equations can be simplified algebraically (similar to Padovani et al. 2014). In the low density regime, where recombinations of electrons and ions are inefficient, we simplify the equations by ignoring the grain-grain CT terms in Eq. 13 and Eq. 14. When electrons are mostly recombined (solution of  $n(e^-) \rightarrow 0$ ), we approximate the abundance of electrons by a simple power law  $x(e^-) \propto (n(\text{H}_2)/\zeta^{\text{H}_2})^{-1}$  (Umebayashi & Nakano 1990), hence to simplify the equations for the high density regime. Note that the boundary between low and high density regimes is grain-size dependent.

The solution to our chemical network requires no iteration in low density regimes, and up to  $\sim 20$  iterations (depending on accuracy) in high density regimes. The low computational cost of the network makes it suitable for solving chemistry along with hydrodynamics during run-time (see the next section § 2.3).

### 2.3 Non-ideal MHD Diffusivity

The evolution of magnetic field in magnetohydrodynamics is governed by the induction equation,

$$\frac{\partial \mathbf{B}}{\partial t} = \nabla \times (\mathbf{v} \times \mathbf{B}) - \nabla \times \left\{ \eta_{\text{Ohm}} \nabla \times \mathbf{B} + \eta_{\text{Hall}} (\nabla \times \mathbf{B}) \times \frac{\mathbf{B}}{B} + \eta_{\text{AD}} \frac{\mathbf{B}}{B} \times \left[ (\nabla \times \mathbf{B}) \times \frac{\mathbf{B}}{B} \right] \right\}, \quad (17)$$

where  $\mathbf{v}$  is the fluid velocity, and  $\eta_{\text{Ohm}}$ ,  $\eta_{\text{Hall}}$ , and  $\eta_{\text{AD}}$  are the Ohmic, Hall, and ambipolar diffusivities, respectively. The three non-ideal MHD coefficients can be expressed in terms of the components of

the conductivity tensor  $\sigma$  (e.g., Wardle 2007):

$$\eta_{\text{AD}} = \frac{c^2}{4\pi} \left( \frac{\sigma_{\text{P}}}{\sigma_{\text{P}}^2 + \sigma_{\text{H}}^2} - \frac{1}{\sigma_{\parallel}} \right), \quad (18)$$

$$\eta_{\text{Ohm}} = \frac{c^2}{4\pi\sigma_{\parallel}}, \quad (19)$$

$$\eta_{\text{Hall}} = \frac{c^2}{4\pi} \left( \frac{\sigma_{\text{H}}}{\sigma_{\text{P}}^2 + \sigma_{\text{H}}^2} \right); \quad (20)$$

where the parallel  $\sigma_{\parallel}$ , Pedersen  $\sigma_{\text{P}}$ , and Hall  $\sigma_{\text{H}}$  conductivities are related to the Hall parameter  $\beta_{i,\text{H}_2}$  as:

$$\sigma_{\parallel} = \frac{ecn(\text{H}_2)}{B} \sum_i Z_i x_i \beta_{i,\text{H}_2}, \quad (21)$$

$$\sigma_{\text{P}} = \frac{ecn(\text{H}_2)}{B} \sum_i \frac{Z_i x_i \beta_{i,\text{H}_2}}{1 + \beta_{i,\text{H}_2}^2}, \quad (22)$$

$$\sigma_{\text{H}} = \frac{ecn(\text{H}_2)}{B} \sum_i \frac{Z_i x_i}{1 + \beta_{i,\text{H}_2}^2}; \quad (23)$$

(Norman & Heyvaerts 1985; Wardle & Ng 1999), where  $x_i$  is the abundance of charged species  $i$ . The Hall parameter  $\beta_{i,\text{H}_2}$  is the key quantity that determines the relative importance of the Lorentz and drag forces in balancing the electric force for each charged species  $i$  in a sea of neutral  $\text{H}_2$  molecules. It is defined as:

$$\beta_{i,\text{H}_2} = \left( \frac{Z_i e B}{m_i c} \right) \frac{m_i + m_{\text{H}_2}}{\mu m_{\text{H}} n(\text{H}_2) < \sigma v >_{i,\text{H}_2}}, \quad (24)$$

where  $m_i$  and  $Z_i e$  are the mass and the charge of charged species  $i$ , respectively, and  $< \sigma v >_{i,\text{H}_2}$  is the momentum transfer rate coefficient, parametrized as a function of temperature (Pinto & Galli 2008), which quantifies the collisional coupling between neutral ( $\text{H}_2$ ) and charged ( $i$ ) species. Note that the momentum transfer rate coefficient  $\beta_{g^-, \text{H}_2}$  and  $\beta_{g^+, \text{H}_2}$  for charged grain species  $g^-$  and  $g^+$  are also averaged over the MRN distribution similar to the recombination rates (Eq. 8).

The solution to our equilibrium chemistry network (§ 2.2) provides the abundances for charged ion and grain species, which are used to update the non-ideal MHD coefficients (from the above equations Eq. 18-24) at each point in the computational domain. The set-up of numerical simulation is described next (§ 3).

## 3 INITIAL CONDITION

We carry out two-dimensional (2D) axisymmetric numerical simulations using ZeusTW code (Krasnopolsky et al. 2010) – a Zeus family MHD code including self-gravity and all three non-ideal MHD effects. The MHD is solved through constraint transport method to preserve the divergence-free condition for magnetic field. We implement a Lorentz force limiter similar to Miller & Stone (2000) to avoid huge Alfvén speed in the low-density bipolar region. The chemistry network is solved at every hydrodynamic timestep, and at each spatial point to compute the non-ideal MHD coefficients. In this study, we consider only ambipolar diffusion and Ohmic dissipation for diffusion of magnetic field (i.e., the second term inside the curly braces in Eq. 17 is neglected). The Hall effect will be addressed in future studies. To avoid extremely small timesteps, we cap the Ohmic diffusivity at  $1.0 \times 10^{20} \text{ cm}^2 \text{ s}^{-1}$ .

We initialize a uniform, isolated spherical core with total mass  $M_c = 1.0 M_{\odot}$ , and radius  $R_c = 10^{17} \text{ cm} \approx 6684 \text{ AU}$ . This corresponds to an initial mass density  $\rho_0 = 4.77 \times 10^{-19} \text{ g cm}^{-3}$  and a volume density for molecular hydrogen  $n(\text{H}_2) = 10^5 \text{ cm}^{-3}$  (assuming mean molecular weight  $\mu = 2.36$ ). The free-fall time of the

**Table 1.** Model Parameters for strong B-field  $B_0 = 42.5 \mu\text{G}$  ( $\lambda=2.4$ )

Model	Grain Size	$\zeta_0^{\text{H}_2}$ $10^{-17} \text{ s}^{-1}$	$\beta_{\text{rot}}$	RSD	Disk Radius AU
Slw-MRN5	MRN	5	.025	N	–
Slw-trMRN5	tr-MRN	5	.025	N <sup>Trans</sup>	$\lesssim 12 \rightarrow 0$
Slw-LG5	LG	5	.025	N <sup>Trans</sup>	$< 5 \rightarrow 0$
Slw-MRN1 <sup>R</sup>	MRN	1	.025	N <sup>Trans</sup>	$\lesssim 9 \rightarrow 0$
Slw-trMRN1	tr-MRN	1	.025	<b>Y</b>	<b><math>\sim 20 \text{ ID}</math></b>
Slw-LG1	LG	1	.025	N <sup>Trans</sup>	$\lesssim 11 \rightarrow 0$
Fst-MRN5	MRN	5	.1	N <sup>Trans</sup>	$\lesssim 10 \rightarrow 0$
Fst-trMRN5	tr-MRN	5	.1	<b>Y</b> <sup>Shrink</sup> <sub>4.7 kyr</sub>	$\lesssim 18 \rightarrow 12$
Fst-LG5	LG	5	.1	N <sup>Trans</sup>	$\lesssim 13 \rightarrow 0$
Fst-MRN1	MRN	1	.1	N <sup>Trans</sup>	$\lesssim 11 \rightarrow 0$
Fst-trMRN1	tr-MRN	1	.1	<b>Y</b>	<b><math>\sim 40 \text{ ID+OR}</math></b>
Fst-LG1	LG	1	.1	<b>Y</b> <sup>Shrink</sup> <sub>5.7 kyr</sub>	$\lesssim 18 \rightarrow 7$

\*Slw-MRN1<sup>R</sup> is the reference model; other symbols are explained in Table 2.

core is thus  $t_{\text{ff}} = 3 \times 10^{12} \text{ s} \approx 9.6 \times 10^4 \text{ yr}$ . We assume an isothermal equation of state below a critical density  $\rho_{\text{cr}} = 10^{-13} \text{ g cm}^{-3}$ , and  $P \propto \rho^{5/3}$  at densities above. <sup>3</sup> The ratio of thermal to gravitational energy is  $\alpha_{\text{thm}} = \frac{5R_{\text{c}}c_s^2}{2GM_{\text{c}}} = 0.75$ , in which  $c_s = 0.2 \text{ km s}^{-1}$  is the isothermal sound speed. The core is rotating initially as a solid-body with angular speed  $\omega_0 = 1 \times 10^{-13} \text{ s}^{-1}$  for slow rotating case, and  $2 \times 10^{-13} \text{ s}^{-1}$  for fast rotating case, which corresponds to a ratio of rotational to gravitational energy  $\beta_{\text{rot}} = \frac{R_{\text{c}}^2\omega_0^2}{3GM_{\text{c}}} = 0.025$  and 0.1, respectively (within range of the typical  $\beta_{\text{rot}}$  estimated by Goodman et al. (1993); Caselli et al. (2002b)). The initial core is threaded by a uniform magnetic field along the rotation axis with a constant strength of  $B_0 \approx 2.13 \times 10^{-5} \text{ G}$  for weak field case and  $4.25 \times 10^{-5} \text{ G}$  for strong field case, which corresponds to a mass-to-flux ratio of  $\lambda = 4.8$  and  $\lambda = 2.4$ , respectively. The strong field case is particularly consistent with the mean value of  $\lambda$  inferred from the OH Zeeman observations by Troland & Crutcher (2008).

We adopt the spherical coordinate system ( $r, \theta$ ) and non-uniform grid to provide high resolution towards the innermost region of simulation domain. The inner boundary has a radius  $r_{\text{in}} = 3 \times 10^{13} \text{ cm} = 2 \text{ AU}$  and the outer has  $r_{\text{out}} = 10^{17} \text{ cm}$ . At both boundaries, we impose a standard outflow boundary conditions to allow matter to leave the computational domain. The mass accreted across the inner boundary is collected at the center as the stellar object. We use a total of  $120 \times 96$  grid points. The grid is uniform in the  $\theta$ -direction, and is non-uniform in the  $r$ -direction with a spacing  $\delta r = 0.1 \text{ AU}$  next to the inner boundary. The spacing increases geometrically outward by a constant factor of  $\sim 1.0647$ .

In this study, we investigate two typical cosmic-ray ionization rate  $\zeta_0^{\text{H}_2} = 1.0 \times 10^{-17} \text{ s}^{-1}$  and  $5.0 \times 10^{-17} \text{ s}^{-1}$ , along with different levels of initial rotation and magnetization, and focus on the effect of dust grain size on the formation of RSDs. The simulation models are summarized in Table 1–2.

<sup>3</sup> In general, the adiabatic index varies with density. For the density range considered in this study ( $n(\text{H}_2) \lesssim 10^{13} \text{ cm}^{-3}$  or  $\rho \lesssim 4 \times 10^{-11} \text{ g cm}^{-3}$ ), gas temperature is well below  $\sim 200\text{--}300 \text{ K}$  almost everywhere. Therefore, molecular hydrogen still behaves like monatomic gas with an adiabatic index of  $5/3$  (Masunaga & Inutsuka 2000; Tomida et al. 2013).

**Table 2.** Model Parameters for weak B-field  $B_0 = 21.3 \mu\text{G}$  ( $\lambda=4.8$ )

Model	Grain Size	$\zeta_0^{\text{H}_2}$ $10^{-17} \text{ s}^{-1}$	$\beta_{\text{rot}}$	RSD	Disk Radius AU
Slw-MRN5	MRN	5	.025	N <sup>Trans</sup>	$\lesssim 14 \rightarrow 0$
Slw-trMRN5	tr-MRN	5	.025	<b>Y</b> <sup>Shrink</sup> <sub>6.7 kyr</sub>	$\lesssim 21 \rightarrow 15$
Slw-LG5	LG	5	.025	N <sup>Trans</sup>	$\lesssim 14 \rightarrow 0$
Slw-MRN1	MRN	1	.025	<b>Y</b> <sup>Shrink</sup> <sub>4.1 kyr</sub>	$\lesssim 16 \rightarrow 9$
Slw-trMRN1	tr-MRN	1	.025	<b>Y</b>	<b><math>\sim 35 \text{ ID+OR}</math></b>
Slw-LG1	LG	1	.025	<b>Y</b> <sup>Shrink</sup> <sub>6.0 kyr</sub>	$\lesssim 19 \rightarrow 13$
Fst-MRN5	MRN	5	.1	N <sup>Trans</sup>	$\lesssim 20 \rightarrow 0$
Fst-trMRN5	tr-MRN	5	.1	<b>Y</b> *	$\lesssim 35 \rightarrow 16 \text{ ID}$
Fst-LG5	LG	5	.1	N <sup>Trans</sup>	$\lesssim 15 \rightarrow 0$
Fst-MRN1	MRN	1	.1	<b>Y</b> <sup>Shrink</sup> <sub>6.3 kyr</sub>	$\lesssim 25 \rightarrow 10$
Fst-trMRN1	tr-MRN	1	.1	<b>Y</b>	<b><math>\sim 40\text{--}60 \text{ OR}</math></b>
Fst-LG1	LG	1	.1	<b>Y</b> <sup>Shrink</sup> <sub>7.5 kyr</sub>	$\lesssim 30 \rightarrow 13$

† MRN: full MRN distribution with  $a_{\text{min}} = 0.005 \mu\text{m}$ ,  $a_{\text{max}} = 0.25 \mu\text{m}$

† tr-MRN: truncated MRN with  $a_{\text{min}} = 0.1 \mu\text{m}$ ,  $a_{\text{max}} = 0.25 \mu\text{m}$

† LG: large grain of single size  $a = 1.0 \mu\text{m}$

† N<sup>Trans</sup>: a transient disk forms from “first core”-like structure, not rotationally supported for most of its lifetime, and disappears quickly in  $\sim$ few  $10^2$  years.

† **Y**<sup>Shrink</sup>: initially forms a RSD but shrinks in size over time (estimated lifetime  $\sim$ few  $10^3$  years).

† **Y**\*: an intermediate type of RSD, shrinking in size over 16 kyrs. The final disk radius holds around  $\sim 16 \text{ AU}$ .

† ID: inner rotationally supported disk.

† OR: outer self-gravitating ring.

#### 4 ANALYTICAL RESULTS OF CHEMISTRY MODEL

In this section, we discuss the results from our analytic chemistry model, with a particular focus on the enhancement of AD by changing dust grain size. The numerical results from ZeusTW simulations are presented in the next section.

To illustrate the effect of dust grain size on magnetic diffusivities, we use the charge abundances solved by our chemistry network (§ 2.2) plus a simple field strength-density relation

$$|B| = 0.143 \left[ \frac{n(\text{H}_2)}{\text{cm}^{-3}} \right]^{0.5} \mu\text{G}, \quad (25)$$

(Nakano et al. 2002), to estimate analytically the three non-ideal MHD coefficients,  $\eta_{\text{AD}}$ ,  $\eta_{\text{Ohm}}$ , and  $\eta_{\text{Hall}}$ . Note that the magnetic field strength will be computed self-consistently in our simulations.

We here compare three cases in terms of chemical abundances and magnetic diffusivities: a) full MRN distribution with  $a_{\text{min}} = 0.005 \mu\text{m}$ , b) truncated MRN (tr-MRN) distribution with  $a_{\text{min}} = 0.1 \mu\text{m}$ , and c) large grains (LG) of single size  $a = 1.0 \mu\text{m}$ . The cosmic-ray ionization rate is set at  $\zeta_0^{\text{H}_2} = 1.0 \times 10^{-17}$  or  $5.0 \times 10^{-17} \text{ s}^{-1}$ , with attenuation prescribed by Eq. 1.

##### 4.1 Fractional Abundance

Fig. 1 shows the fractional abundances of charged gas-phase species and dust grains for the three grain size cases (MRN, tr-MRN, and LG), from which the following trends are evident.

*First*, in the MRN case, charges are mainly dominated by  $e^-$ ,  $m^+$ , and to a lesser extent  $M^+$  in the low density regime ( $\lesssim 10^7 \text{ cm}^{-3}$ ), and by charged grains  $g^-$  and  $g^+$  in the high density regime ( $\gtrsim 10^9 \text{ cm}^{-3}$ ), with a transition region in between when recombination of  $e^-$  starts to become very efficient. In the tr-MRN



ple, the magnitude of  $\eta_{AD}$  in the LG case (shown in Fig 2, in between the other two cases) is roughly comparable to that of  $a_{\min} \approx 0.04 \mu\text{m}$  in the low density regime ( $\lesssim 10^{10} \text{ cm}^{-3}$ ); but it is  $\sim 10$ – $100$  times smaller at high densities ( $\gtrsim 10^{10} \text{ cm}^{-3}$ ) than that of the small grain cases due to insufficient recombination of ions and electrons on grain surfaces. For even larger grains (of single size  $\gtrsim 10^1 \mu\text{m}$ ), their  $\eta_{AD}$  are roughly comparable to that of  $a_{\min} \approx 0.03 \mu\text{m}$ , which are still bigger than that of the MRN case in low density regimes.

- From  $a_{\min} \approx 0.1 \mu\text{m}$  down to  $a_{\min} \approx 0.01 \mu\text{m}$ , the  $\eta_{AD}$  curve drops down because of the rapid increase in the Hall conductivity  $\sigma_H$  (Eq. 18), which is determined by negatively charged grains (see § 4.4). Here, the increase in  $\sigma_H$  is mainly caused by the increase in the abundance of negatively charged grains  $x(g^-)$ . When  $a_{\min} \lesssim 0.04 \mu\text{m}$ ,  $\sigma_H$  rises above  $\sigma_P$  between  $n(\text{H}_2) \sim 10^6$ – $10^{11} \text{ cm}^{-3}$ . Below  $a_{\min} \approx 0.02 \mu\text{m}$ , negatively charged grains start to dominate the Pedersen conductivity  $\sigma_P$  as well at low densities. These small size grains ( $10$ – $200 \text{ \AA}$ ), relatively well-coupled to the magnetic field ( $|\beta_{g^-, \text{H}_2}|$  around unity), can exert stronger drag to  $\text{H}_2$  molecules than ions and electrons do (Pinto et al. 2008). A large number of such grains (by reducing  $a_{\min}$ ) therefore dominate the conductivity  $\sigma_P$  (e.g., see Fig. 5 in § 4.4).

- There exists a “worst grain size”  $a_{\min} \approx 0.01 \mu\text{m}$  that produces an overall lowest ambipolar diffusivity in the low density regime, with a minimum of  $\eta_{AD} \sim 10^{17} \text{ cm}^2 \text{ s}^{-1}$  between  $n(\text{H}_2) \sim 10^8$ – $10^9 \text{ cm}^{-3}$ . This is because the Hall conductivity (Eq. 18) reaches a maximum, which is  $\gtrsim 1$  order of magnitude higher than the Pedersen conductivity at densities between  $\sim 10^8$ – $10^9 \text{ cm}^{-3}$ .

- From  $a_{\min} \approx 0.01 \mu\text{m}$  down to  $a_{\min} \approx 0.003 \mu\text{m} = 30 \text{ \AA}$ , the  $\eta_{AD}$  curve lifts up slightly between  $n(\text{H}_2) \sim 10^7$ – $10^9 \text{ cm}^{-3}$  as Pedersen conductivity  $\sigma_P$  starts to increase (both  $x(g^-)$  and  $|\beta_{g^-, \text{H}_2}|$  increases) and Hall conductivity  $\sigma_H$  remains relatively unchanged ( $|\beta_{g^-, \text{H}_2}|$  becomes larger than 1 and offsets the increase in  $x(g^-)$ ). Note that in this size range  $\sigma_P \ll \sigma_H$  at low densities.

- Below  $a_{\min} \approx 30 \text{ \AA}$ ,  $\sigma_P$  finally becomes larger than  $\sigma_H$  again, and the  $\eta_{AD}$  curve slowly rises as both Pedersen and Hall conductivities gradually decrease due to the increasing  $|\beta_{g^-, \text{H}_2}|$ . Note that the PAH-type grains with size  $10 \text{ \AA}$  or less have Hall parameter comparable to that of ions. However, even with  $a_{\min} \approx 4 \text{ \AA}$  (smallest possible grain size Weingartner & Draine 2001), the  $\eta_{AD}$  curve only returns to the level of  $a_{\min} \approx 0.03 \mu\text{m}$  in low density regimes.

We also investigate other maximum grain sizes  $a_{\max}$ . For example, when  $a_{\max} = 1 \mu\text{m}$ , the optimal  $a_{\min}$  that yields the largest AD enhancement is reduced to  $\approx 0.055 \mu\text{m}$ . Besides, the overall  $\eta_{AD}$  curve with  $[0.055 \mu\text{m}, 1 \mu\text{m}]$  is slightly lower than the  $[0.1 \mu\text{m}, 0.25 \mu\text{m}]$  curve. The reason is that, large  $a_{\max}$  reduces the total grain surface area for recombination; thus to suppress the excessive ions and electrons, one needs to add back more small grains to restore enough grain surface area. But too many small grains of few  $100 \text{ \AA}$  will instead reduce  $\eta_{AD}$  because they dominates the fluid conductivity, especially when  $a_{\min} \lesssim 0.02 \mu\text{m}$ .

The differences in Ohmic diffusivity  $\eta_{\text{Ohm}}$  are also prominent among all cases. Fig. 2 shows that grain size anti-correlates with Ohmic diffusivity  $\eta_{\text{Ohm}}$ . The main current carrier — electrons — are responsible for the strength of Ohmic dissipation. As grain size increases, the recombination of electrons becomes less efficient due to a smaller total grain surface area, which boosts the fluid conductivity (see § 4.4 for detailed analysis) and suppresses the Ohmic diffusivity. Note that the Ohmic dissipation in Fig. 2 only starts to strongly affect the diffusion of magnetic fields at high densities  $n(\text{H}_2) \gtrsim 10^{11} \text{ cm}^{-3}$ , below which AD and Hall effect dominate (con-

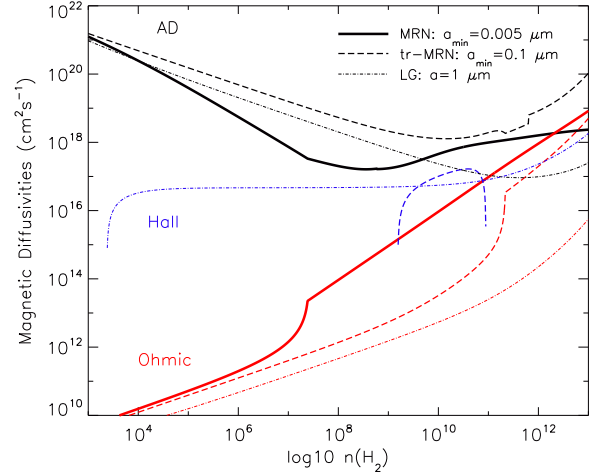


**Figure 3.** Magnetic diffusivities for different cases of grain size with  $\zeta_0^{\text{H}_2} = 5.0 \times 10^{-17} \text{ s}^{-1}$ , for the illustrative magnetic field-density relation given in Eq. 25. The Hall diffusivity in the MRN case are negative within the density range.

sistent with existing literature, e.g., Kunz & Mouschovias 2010; Li et al. 2011).

Our result also shows that the relative importance between Ohmic dissipation and AD varies with grain size distribution. In the standard MRN case, Ohmic dissipation dominates over AD when  $n(\text{H}_2) \gtrsim \text{few } 10^{11} \text{ cm}^{-3}$ . In contrast, in both tr-MRN and LG cases, ambipolar diffusivity  $\eta_{AD}$  is always orders of magnitude larger than Ohmic diffusivity  $\eta_{\text{Ohm}}$  for the density range in this study ( $\lesssim 10^{13} \text{ cm}^{-3}$ ). Our chemistry model indicates that such a result also holds for other values of  $a_{\min}$  as long as  $a_{\min} \gtrsim 0.02 \mu\text{m}$ . Particularly, the strong AD in the tr-MRN case at high densities ( $\sim 10^{11}$ – $10^{13} \text{ cm}^{-3}$ ) is caused by the lack of highly conductive VSGs which dominate the Pedersen conductivity  $\sigma_P$  in the MRN case (§. 4.4, see also Desch & Mouschovias 2001; Dapp et al. 2012).

### 4.3 Effect of Cosmic-ray Ionization Rate

The charge abundances and hence magnetic diffusivities also depend on the cosmic-ray ionization rate. Our chemistry model shows that the magnetic diffusivity scales with cosmic-ray ionization rate roughly as  $\propto \sqrt{\zeta^{\text{H}_2}}$  (see Fig. 3). Though the effect varies somewhat with density, it largely agrees with theoretical prediction (Shu 1991). The factor of  $\sim 2$  difference in magnetic diffusivities, by changing  $\zeta_0^{\text{H}_2}$  from  $1.0 \times 10^{-17} \text{ s}^{-1}$  to  $5.0 \times 10^{-17} \text{ s}^{-1}$ , will also play a role in the formation of RSDs (see Table 1-2 and § 5.4). Its role is not as decisive as that of the grain size, but can greatly affect the age and morphology of disks and is more important than parameters other than grain size.

### 4.4 Analysis of Conductivity

In this section, we will elaborate on the conductivity of charged species to provide a more thorough explanation for the results above. The bottom line is that: 1) both the fractional abundances of charged species (§ 4.1) and their Hall parameters (Eq. 24) are important to fluid conductivity; and 2) a large population of con-

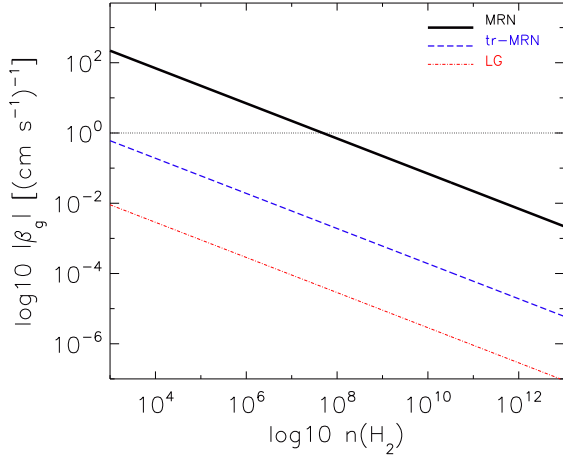


**Figure 4.** Hall parameter  $|\beta_{g-H_2}|$  for different cases of grain size, the values in the MRN and tr-MRN cases are averaged over the size distribution. Horizontal dotted line indicates Hall parameter of unity.

ductive VSGs in MRN distribution greatly reduces the ambipolar diffusivity  $\eta_{AD}$ .

In general, each charged species is coupled to the magnetic field by the Lorentz force to certain extent; the degree of decoupling is determined by the drag force exerted through collision with neutrals. The relative importance of the Lorentz force versus drag force is quantified through the Hall parameter  $\beta_{i,H_2}$ . Ions and electrons couple more strongly to the magnetic field owing to their light weight and small collisional cross-section. For charged grains, the coupling to the magnetic field depends on the grain size; smaller size grains are better-coupled than larger ones. Although the grain-field coupling is generally weaker than the ion-(electron)-field coupling, however, grains exert much stronger drag to their surrounding neutral molecules than ions and electrons do (Pinto et al. 2008). Nevertheless, the grain’s Hall parameter  $|\beta_{g-H_2}|$  is a good indicator of the two competing effects, which is plotted in Fig. 4 for the three grain size cases MRN, tr-MRN, and LG (averaged over the size distribution).

The comparison of  $|\beta_{g-H_2}|$  for different grain sizes clearly shows the  $\propto a^{-2}$  dependence due to the inverse of momentum transfer rate  $\langle \sigma v \rangle^{-1}$ . The overall magnitude of  $|\beta_{g-H_2}|$  in the MRN case is  $\sim 20^2$  times of that in tr-MRN case; and the value in tr-MRN case is  $\sim 10^2$  times of that in LG case. In the MRN case,  $|\beta_{g-H_2}|$  is well above 1 at low densities ( $n(H_2) \lesssim 10^7 \text{ cm}^{-3}$ ), implying a strong coupling to the magnetic field from the large population of small grains. The coupling only weakens at high densities after  $|\beta_{g-H_2}|$  drops below unity. For the tr-MRN and LG cases, however, the Hall parameter is well below 1 for all densities, suggesting that the drag force exerted on grains by grain-neutral collision always dominates the Lorentz force. The large difference in the Hall parameter of charged grains strongly affects the conductivities, especially the Pedersen conductivity  $\sigma_P$  (Fig. 5-7); it is one of the key origins for the AD enhancement (§ 4.2).

Comparing Fig. 5 and Fig. 6, the most notable difference is the  $g^-$ ’s contribution to the Pedersen conductivity  $\sigma_P$ .

- In the MRN case, the  $\sigma_P$  is entirely determined by the component from negatively charged grains  $\sigma_P(g^-)$ , whose value is over 1–2 orders of magnitude higher than that of molecular ions  $\sigma_P(m^+)$ ,

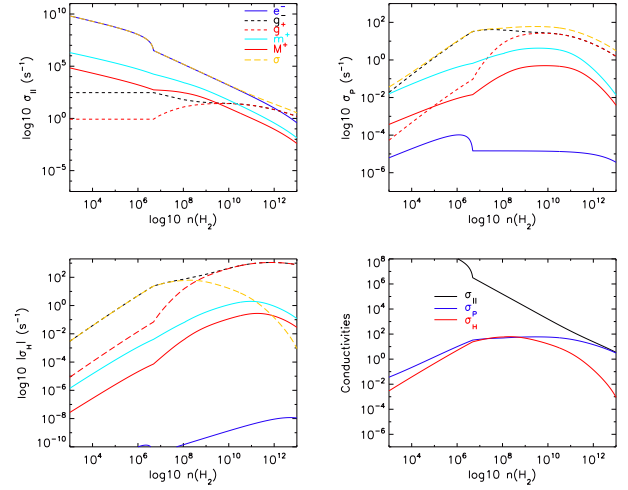


**Figure 5.** Parallel  $\sigma_{||}$  (top-left), Pedersen  $\sigma_P$  (top-right), and Hall  $\sigma_H$  (bottom-left) components of the conductivity tensor, and contributions made by different species to each conductivity component for the MRN grain size distribution. Bottom-right panel plots the three conductivity components together, which are shown as  $\sigma$  (yellow dashed lines) in the other three panels respectively. The computation adopts the illustrative magnetic field-density relation given in Eq. 25.

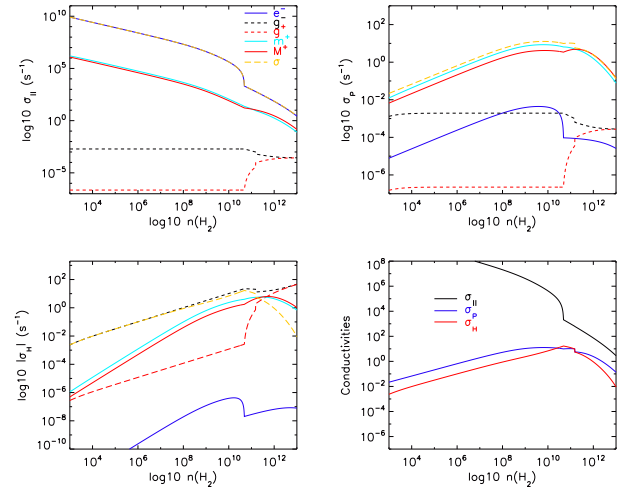


**Figure 6.** As for Fig. 5, but for tr-MRN grain size distribution.

and about 3 orders of magnitude higher than that of metal ions  $\sigma_P(m^+)$ ; because the grains, even of small sizes in the MRN case, have significantly smaller Hall parameter than typical ions or electrons. The collisional drag between MRN grains and neutrals is generally stronger than that between ions (electrons) and neutrals. Or mathematically,  $\sigma_P \propto \frac{x_i \beta_{i,H_2}}{(1 + \beta_{i,H_2}^2)}$ , and  $\propto \frac{x_i}{\beta_{i,H_2}}$  for  $\beta_{i,H_2} \gg 1$  (note that the abundances  $x_i$  of ions and grains do not differ much in the intermediate densities  $10^6$ - $10^{10} \text{ cm}^{-3}$  in Fig. 1).

- In the tr-MRN case, in contrast,  $\sigma_P(g^-)$  is about  $10^4$  times smaller than that in the MRN case, and the total Pedersen conductivity  $\sigma_P$  is dominated by molecular and metal ions instead ( $\sim 1$ – $2$  orders of magnitude lower than the MRN value). This is mainly for

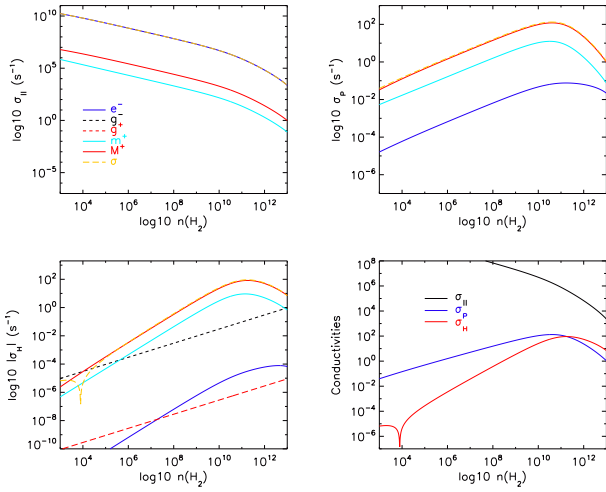


**Figure 7.** As for Fig. 5, but for LG of single size  $1 \mu\text{m}$ .

two reasons. First, the Hall parameter  $\beta_{g^-, \text{H}_2}$  decreases from  $\gg 1$  in the MRN case to  $< 1$  in the tr-MRN case (Fig. 4), which completely changes  $\sigma_{\text{P}}(g^-)$ 's dependence on Hall parameter into  $\sigma_{\text{P}} \propto x(g^-)\beta_{g^-, \text{H}_2}$ . At density  $n(\text{H}_2) \sim 10^7 \text{ cm}^{-3}$  for example,  $\propto \frac{1}{\beta_{g^-, \text{H}_2}}$  in the MRN case gives a value of a few  $10^{-1}$ , and  $\propto \beta_{g^-, \text{H}_2}$  in the tr-MRN case gives a value of  $\sim 10^{-2}$ ; the difference is a factor of a few  $10^1$ . Second, the abundance of negatively charged grains  $x(g^-)$  reduces by  $\approx 500$  times (Fig. 1) when  $a_{\text{min}}$  changes from  $0.005 \mu\text{m}$  (MRN) to  $0.1 \mu\text{m}$  (tr-MRN). Therefore, both a difference in  $\beta_{g^-, \text{H}_2}$  (by order of  $10^1$ ) and a difference in grain abundance  $x(g^-)$  (by order of  $10^2$ ) together lead to the large difference in the grains' Pedersen conductivity  $\sigma_{\text{P}}(g^-)$ . Note that in the LG case,  $\sigma_{\text{P}}(g^-)$  drops below  $10^{-7}$  that it is not shown in Fig. 7.

Due to the smaller Hall parameter of grains than that of ions and electrons, the Hall conductivity  $|\sigma_{\text{H}}|$  is normally dominated by the  $g^-$  component  $|\sigma_{\text{H}}(g^-)|$  as long as grain size is below  $\lesssim 0.5 \mu\text{m}$  (large size grains become much less abundant) and above  $\gtrsim 10 \text{ \AA}$  (PAH-type grains have Hall parameter comparable to that of ions). Comparing Fig. 5 and Fig. 6,  $|\sigma_{\text{H}}(g^-)|$  is larger in the MRN case at densities below  $\sim 10^{10} \text{ cm}^{-3}$ , and is larger in the tr-MRN case at higher densities. As shown in Eq. 23, the Hall conductivity of negatively charged grains depends on their abundance  $x(g^-)$  and Hall parameter  $\beta_{g^-, \text{H}_2}$  as  $|\sigma_{\text{H}}(g^-)| \propto \frac{x(g^-)}{1 + \beta_{g^-, \text{H}_2}^2}$ . When  $n(\text{H}_2) \lesssim 10^6 \text{ cm}^{-3}$ , the abundance  $x(g^-)$  differs by  $\approx 500$  times between the two cases; however, the effect is partly alleviated by the inverse dependence on  $1 + \beta_{g^-, \text{H}_2}^2$ , because  $|\beta_{g^-, \text{H}_2}| \gg 1$  for MRN case but  $\ll 1$  for tr-MRN case. For higher densities,  $|\beta_{g^-, \text{H}_2}|$  drops below unity for both cases and  $|\sigma_{\text{H}}(g^-)|$  becomes roughly proportional to  $x(g^-)$ . The difference in  $|\sigma_{\text{H}}(g^-)|$  between the two cases peaks around number density  $10^7 \text{ cm}^{-3}$ , with the MRN case  $|\sigma_{\text{H}}(g^-)|$  being  $\sim 100$  times larger than that of the tr-MRN case. Between  $10^7$  and  $10^{10} \text{ cm}^{-3}$ , such difference dwindles because the abundance  $x(g^-)$  in the MRN case starts to decline due to efficient grain-grain neutralization, while not for the tr-MRN case yet. At even higher densities  $\gtrsim 10^{10} \text{ cm}^{-3}$ , the Hall conductivity in the tr-MRN case overtakes that in the MRN case, because the canceling effect from positively-charged grains ( $\sigma_{\text{H}}(g^+) \propto x(g^+)$ ) is weaker in the former. Note that in the LG case,  $\sigma_{\text{H}}$  is mostly determined by metal ions, which changes its sign to positive.

The parallel component of the conductivity tensor —  $\sigma_{\parallel}$  — is almost always determined by electrons in all three cases. Recall that  $\sigma_{\parallel} \propto x_i \beta_{i, \text{H}_2}$ . Electron is so light-weighted that its Hall parameter  $\beta_{e^-, \text{H}_2}$  is more than 3 orders of magnitude larger than that of ions, and more than  $10^5$  times than MRN grains ( $10^7$  times than tr-MRN grains). Therefore, electron generally contributes the most to parallel conductivity, as long as its abundance  $x(e^-)$  is not significantly lower than the other charged species. Exception only occurs at very high densities ( $> 10^{12} \text{ cm}^{-3}$ ) in the MRN case, where the abundance of electrons  $x(e^-)$  is  $10^6$ - $10^7$  times lower than the abundances of charged grains; so that both  $g^-$  and  $g^+$  start to dominate  $\sigma_{\parallel}$  near the high density tail (see Fig. 5).

We conclude this section by comparing the three components of the conductivity tensor:  $\sigma_{\parallel}$ ,  $\sigma_{\text{P}}$ , and  $\sigma_{\text{H}}$ . By definition of Eq. 18–20, the strength of each type of magnetic diffusivity is determined by the absolute magnitude as well as the relative importance of the three conductivities, summarized as below (see also Wardle & Ng 1999):

- (i) strong  $\eta_{\text{AD}}$  requires: small  $\sigma_{\text{P}}$  while  $\sigma_{\parallel} \gg \sigma_{\text{P}} \gg |\sigma_{\text{H}}|$ .
- (ii) strong  $\eta_{\text{Ohm}}$  requires: small  $\sigma_{\parallel}$ ; (note that, for Ohmic dissipation to dominate over the other two effects, we need  $\sigma_{\parallel}$  slightly  $> \sigma_{\text{P}} \gg |\sigma_{\text{H}}|$ .)
- (iii) strong  $\eta_{\text{Hall}}$  requires: small  $|\sigma_{\text{H}}|$  while  $|\sigma_{\text{H}}| \gg \sigma_{\text{P}}$ ; (note that, for Hall effect to dominate, we need  $\sigma_{\parallel} \gg |\sigma_{\text{H}}|$ .)

The AD enhancement seen in the tr-MRN case exactly matches the criteria in (i). As discussed above, the small Pedersen conductivity  $\sigma_{\text{P}}$  owes to the removal of a large amount of conductive VSGs, so that both the abundance and Hall parameter of grains become low. Hence only ions ( $m^+$  and  $M^+$ ) dominate  $\sigma_{\text{P}}$ . The relation  $\sigma_{\parallel} \gg \sigma_{\text{P}} \gg |\sigma_{\text{H}}|$  is also satisfied for most densities because  $|\sigma_{\text{H}}|$  — primarily controlled by grains — plunged with the low grain abundance, and  $\sigma_{\parallel}$  — controlled by electrons — are always orders of magnitude larger than the other two conductivities.

In the MRN case, the conductivities satisfy the criteria in (ii) at high densities ( $\gtrsim \text{few } 10^{11} \text{ cm}^{-3}$ ); however, at lower densities, although AD dominates the magnetic diffusion, the strength of  $\eta_{\text{AD}}$  is weaker by  $\sim 1$ – $2$  orders of magnitude than that of the tr-MRN case (Fig. 2), owing to the large Pedersen and Hall conductivities here. At densities below  $\sim 10^7 \text{ cm}^{-3}$ , the Pedersen conductivity  $\sigma_{\text{P}}$  is larger (only slightly) than the Hall conductivity  $|\sigma_{\text{H}}|$ ; but the latter increases with density faster than the former, which undermines  $\eta_{\text{AD}}$  (Eq. 18). Between  $\sim 10^7$  and  $\sim 10^9 \text{ cm}^{-3}$ ,  $\sigma_{\text{P}} \approx |\sigma_{\text{H}}|$ , so that the  $\eta_{\text{AD}}$  curve reaches a minimum. From  $\sim 10^9$  to  $\sim 10^{11} \text{ cm}^{-3}$ ,  $\eta_{\text{AD}}$  starts to increase slightly because  $\sigma_{\text{H}}$  decreases rapidly as a result of efficient grain-grain neutralization, while  $\sigma_{\text{P}}$  does not change much. At high densities  $n(\text{H}_2) \gtrsim 10^{11} \text{ cm}^{-3}$ , Ohmic dissipation becomes the dominant diffusion process. It is mainly caused by the large  $\sigma_{\text{P}}$  that nearly equals  $\sigma_{\parallel}$ , hence the criteria in (ii) are satisfied.

In the LG case, the conductivities satisfy criteria in (i) at low densities ( $\lesssim 10^{11} \text{ cm}^{-3}$ ) and criteria in (iii) at high densities ( $\gtrsim 10^{11} \text{ cm}^{-3}$ ). However, the overall strength of  $\eta_{\text{AD}}$  is  $\sim \text{few}$  times smaller than that in the tr-MRN case, yet still  $\sim \text{few } 10^1$  times bigger than the MRN case in the low density regimes. Here, both Pedersen and Hall conductivities are controlled mostly by metal ions. The Hall conductivity  $\sigma_{\text{H}}$  changes sign at density  $\sim 10^4 \text{ cm}^{-3}$  from  $g^-$  dominated regime into  $M^+$  dominated regime. It increases faster with density than Pedersen conductivity  $\sigma_{\text{P}}$  due to the  $\propto \frac{1}{\beta_{i, \text{H}_2}^2}$  dependence compared with the  $\propto \frac{1}{\beta_{i, \text{H}_2}}$  dependence for  $\sigma_{\text{P}}$  ( $\beta_{M^+, \text{H}_2} \gg 1$  and is decreasing with density). When density

$n(\text{H}_2) \geq 10^{11} \text{ cm}^{-3}$ ,  $\sigma_{\text{H}}$  overtakes  $\sigma_{\text{P}}$ , therefore Hall diffusivity  $\eta_{\text{Hall}}$  becomes the strongest among the three magnetic diffusivities.

## 5 SIMULATION RESULTS

With a better understanding of analytical results from the chemistry model, we present the simulation results in this section, which largely follow the analytical expectations above. In comparison, the numerical simulation offers more realistic strength and geometry of the magnetic field than the simple relation Eq. 25 used in the previous section. It also allows us to study the interplay of different physical processes, and to determine the relative importance of different parameters on disk formation.

As summarized in Table 1-2, a 4-parameter space including magnetic field strength (in terms of mass-to-flux ratio  $\lambda$ ), grain size, cosmic-ray ionization rate, and initial rotation speed (in terms of  $\beta_{\text{rot}}$ ), is explored with a total of 24 calculations. We find that each parameter has an impact on the formation of RSDs and the lifetime of disks. Weaker magnetic field strength, lower cosmic-ray ionization rate, or faster rotation speed all promote disk formation to certain degree (e.g., increase disk size and/or lifetime); however, the most effective is by changing the grain size distribution. Formation of long-lived stable RSDs (even self-gravitating disks and rings) is only possible in the tr-MRN cases, or with similar grain size distributions that are free of a large population of VSGs.

### 5.1 Disk Morphology

The whole parameter space produces 3 major types of disks, categorized based on their lifetime and size as follows:

- (i)  $\text{N}^{\text{Trans}}$  (or N): a small transient disk (not rotationally supported for most of its lifetime) of radius  $\sim 10$  AU forms from “first core”-like structure and disappears quickly within  $\sim \text{few } 10^2$  to  $10^3$  years due to accretion of low angular momentum gas.
- (ii)  $\text{Y}_{t_{\text{d}}}^{\text{Shrink}}$ : a RSD of radius  $\sim 20$  AU is able to form from initial collapse; but its size shrinks over time, with a lifetime  $t_{\text{d}} \sim \text{few } 10^3$  to  $10^4$  years.
- (iii) Y: large RSDs of radius  $\sim 20$ – $50$  AU are able to form and survive (at least  $\text{few } 10^4$  years). The disk maintains a relatively stable size by accreting high angular momentum gas; its mass can grow up to 30%–40% of the total core mass.

Type (iii) disk only forms when the grain size distribution is a truncated MRN. Depending on different combinations with other parameters, such disks in 2D can have substructures including *ID* — small Keplerian inner disk around the central star, and *OR* — massive rotationally supported outer ring at the centrifugal barrier, which is an evolutionary outcome of a single disk that forms first.

The categorization criteria above are not strict. Some type (i) transient disks ( $\text{N}^{\text{Trans}}$ ) in the weaker B-field ( $\lambda = 4.8$ ) cases do partly become rotationally supported for a small fraction of their lifetime. Another example is the intermediate type of RSD formed in the  $\lambda = 4.8$  Fst-trMRN5 case which, despite shrinking in size, can survive a much longer time ( $> 16$  kyr); and the disk radius holds steady around 16 AU at the end of the simulation. It is possible that, as more parameter space is explored, the category boundary can become less sharp.

### 5.2 AD-Enabled Disk Formation: from MRN to tr-MRN

The formation of long-lived RSDs in the tr-MRN runs is essentially caused by the enhanced AD as shown in the analytical result § 4.2. The strong AD weakens the coupling of neutral gas to magnetic field and reduces the amount of magnetic flux being dragged in by the collapsing flow. Therefore, magnetic braking is weakened, especially in the circumstellar region, and sufficient angular momentum can be preserved for a rotationally supported disk. To illustrate this, we compare the reference model Slw-MRN1<sup>R</sup> (Fig. 9) with model Slw-trMRN1 (Fig. 12), both for the strong initial B-field  $\lambda = 2.4$ .

#### 5.2.a MRN Grain Reference Model: $\lambda 2.4$ Slw-MRN1<sup>R</sup>

The reference model Slw-MRN1<sup>R</sup> is representative of the type (i) transient disks in this study; it is also considered as a standard case in other disk formation studies (e.g., Li et al. 2011; Tomida et al. 2013; Masson et al. 2015). Although a RSD is frequently claimed to form from Larson’s first core (e.g., Machida & Matsumoto 2011; Tomida et al. 2013; Tsukamoto et al. 2015a), these studies do not follow the disk evolution very long. Hence, there is no direct evidence that the small disk formed from the first core can survive or grow in size by accreting infalling gas with enough angular momentum.

As shown in the middle panel of Fig. 8, a spherical structure ( $\lesssim 10$  AU) similar to the Larson’s first core do appear at  $t \approx 165.1$  kyr ( $\sim 1.7 t_{\text{ff}}$ , middle panel), with a  $0.002 M_{\odot}$  ( $\sim 2$  Jupiter mass) stellar object in its center. Because we do not treat the full radiative transfer in our study, formation of this structure owes to the stiffening of the equation of state, i.e., transitioning from isothermal to adiabatic regime. In the central part of the structure, the temperature reaches a few  $10^2$  K. The inner  $\sim 8$  AU is rotating temporarily faster than Keplerian speed as the star mass is still small. On the other hand, the gas at radius beyond 8 AU all rotates with sub-Keplerian speed, indicating a low specific angular momentum in circumstellar regions (see Fig. 14). As these materials fall towards the center, the “first core” structure quickly becomes non-rotationally supported in less than 300 years at  $t \approx 165.4$  kyr. The stellar mass grows to  $0.01 M_{\odot}$ , and the density rarefaction caused by infall carves out the bipolar regions, which is shaping the core into a more disk-like structure. Up to this time, the inner  $\sim 10$  AU is dominated by the thermal pressure  $P_{\text{th}}$ , where the plasma  $\beta$  ( $\equiv \frac{P_{\text{th}}}{P_{\text{B}}}$ ) can reach a few  $10^2$  to  $10^3$ . Unfortunately, this “first core”-like structure lacks further angular momentum supply, which quickly leads to its disappearance in less than 200 years. At  $t \approx 165.6$  kyr (Fig. 9), the whole structure has been accreted by the central star, leaving only a magnetically-dominated pseudo-disk around a  $0.046 M_{\odot}$  star.

In Fig. 9, the magnetic field lines along the equator are strongly pinched towards the central star, with field strength up to  $\sim 1$  G; however, diffusion of magnetic field is inefficient. The Ohmic diffusivity  $\eta_{\text{Ohm}}$  only becomes large ( $\geq 10^{18} \text{ cm}^2 \text{ s}^{-1}$ ) near the surface of the 2 AU inner hole and in the central thin layer of the pseudo-disk, where densities are above  $\text{few } 10^{-12} \text{ g cm}^{-3}$ . The ambipolar diffusivity  $\eta_{\text{AD}}$  is overall low along the equator, implying an inefficient AD. Therefore in this case, decoupling of matter from magnetic field occurs only near the inner hole through Ohmic dissipation, which allows the accretion flow to land onto the central star. Note that the high  $\eta_{\text{AD}}$  in the outflow cavity is because of the low density in these regions.

The non-rotationally-supported nature of the pseudo-disk at

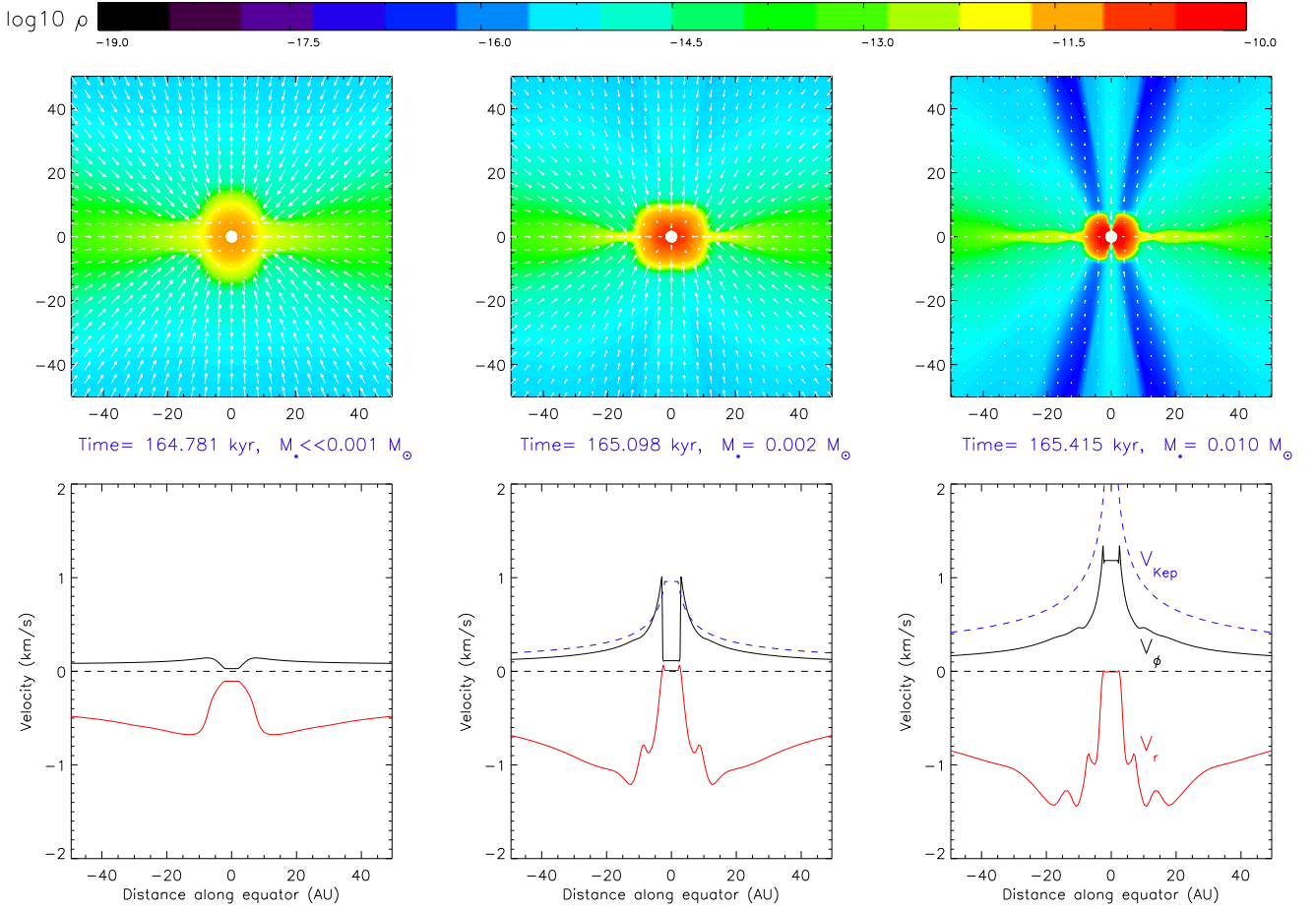


**Figure 8.** Early evolution of density distribution (color map) and velocity field (white arrows) for the  $\lambda 2.4$  Slw-MRN1<sup>R</sup> reference model inside 50 AU radius. The corresponding velocity profiles along the equator are plotted in the bottom panels. Note that the inner hole has a radius of 2 AU.

$t = 165.6$  kyr is also obvious from the velocity profile in Fig. 10. The gas on the pseudo-disk is infalling supersonically towards the central star with increasing  $v_r$ , while the rotation speed  $v_\phi$  is highly sub-Keplerian. No obvious bump in the infall velocity due to AD-shock (Li & McKee 1996; Li et al. 2011) is present in this case, because the stellar mass is still quite low and not much magnetic flux has been decoupled from the accreted matter. The magnetic pressure  $P_B (=|B|^2/(8\pi))$ , ram pressure  $P_{\text{ram}} (= \rho v_r^2)$ , and thermal pressure  $P_{\text{th}}$  are all increasing towards the center. The thermal pressure no longer dominates the inner  $\sim 10$  AU, where the plasma  $\beta$  drops to unity. At this stage, gas on the pseudo-disk has already lost most of its angular momentum through magnetic braking; this results in the fast infall motion of gas and a rapid increase in stellar mass.

### 5.2.b Truncated-MRN Grain Model: $\lambda 2.4$ Slw-trMRN1

In contrast, the  $\lambda 2.4$  Slw-trMRN1 model clearly demonstrates formation of large sustainable RSDs; it also represents the type (iii) disks in this study. As shown in Fig. 11, the central dense structure is persistently super-Keplerian, from the early “first core”-like structure to the well defined disk later on. The “first core”-like structure starts as an elongated shape with radius  $\sim 15$  AU, at  $t \approx 142.6$  kyr ( $\sim 1.5 t_{\text{ff}}$ ). Its innermost  $\sim 10$  AU is close to the shock front created by the centrifugal barrier (see detailed discussion in

§ 5.2.c), therefore both infall and rotation motions are suppressed. However, at larger radius ( $\geq 10$  AU) along the equator, gas rotates with super-Keplerian speed, contrary to that of the reference model. It implies that the infalling gas still retains a relatively high angular momentum (see Fig. 14). As collapse continues, this angular momentum influx is able to spin up the inner  $\sim 15$ – $20$  AU and to enable the formation of a RSD in  $\sim 600$  years ( $t \approx 143.2$  kyr) around a  $0.007 M_\odot$  ( $\sim 7$  Jupiter mass) protostar. Meanwhile, density cavities appear in the bipolar regions as a result of rapid infall onto the flattened equatorial region. However, magnetically driven outflows only appear shortly afterwards (at  $\approx 143.6$  kyr, not shown), which continuously carves the cavity wall as the disk grows in size. The third panel of Fig. 11 captures a representative moment when such magnetically driven outflow is pushing out more materials near the cavity wall and widening the cavity angle. The launching point of the outflow locates at the disk outer edge  $\sim 20$  AU, where gas flow is being accreted onto the disk and field lines are strongly pinched. As evolution continues, the RSD in this model survives beyond 14 kyr with mass growing above  $0.22 M_\odot$ , and shows no sign of disappearing.<sup>4</sup>

<sup>4</sup> We stopped the 2D axisymmetric simulation because of the lack of 3D gravitational and MHD instabilities to redistribute angular momentum in the disk, which is needed for disk accretion onto the central object. As a

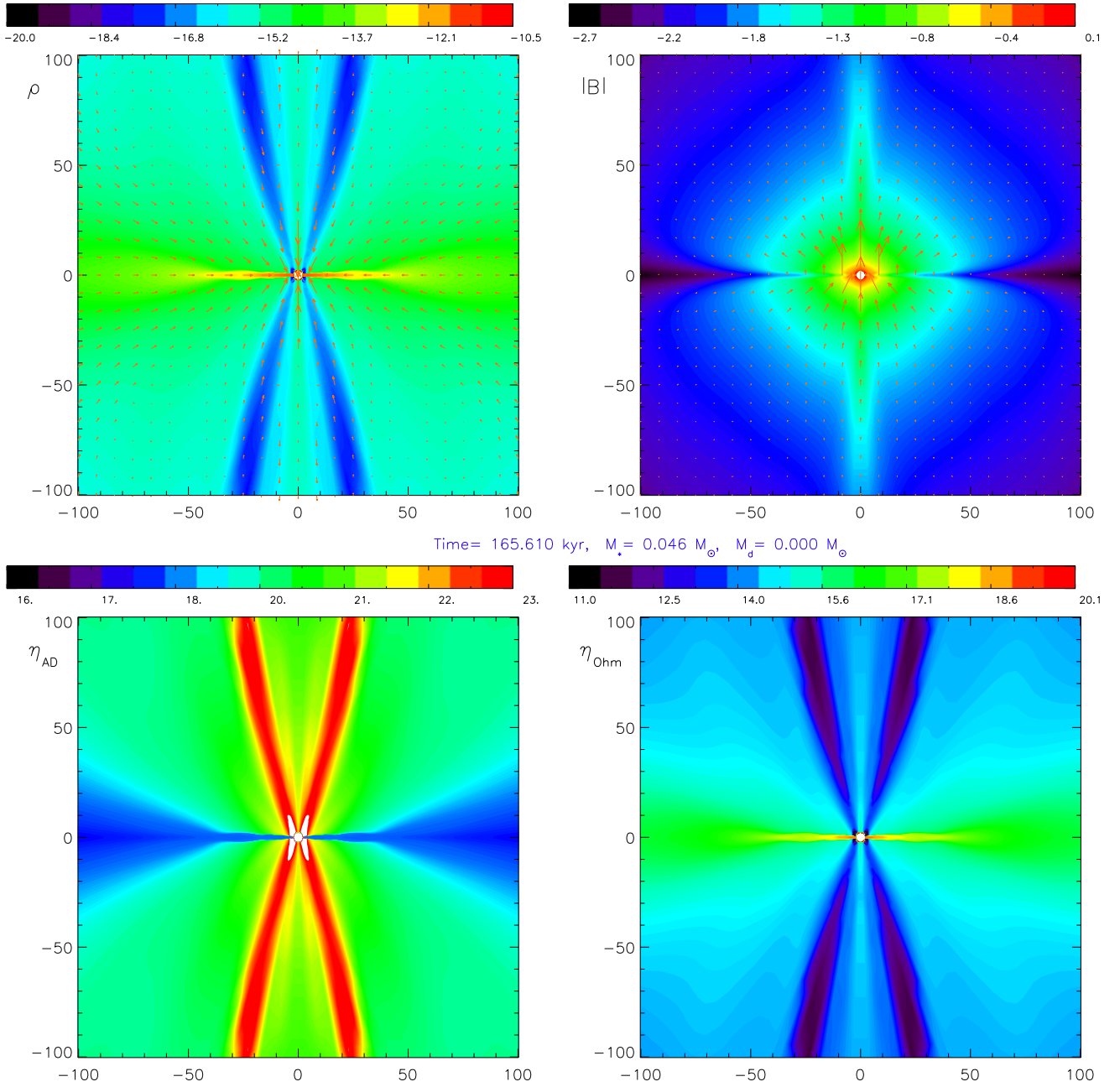


**Figure 9.** Distributions of density  $\rho$ , magnetic field strength  $|B|$ , ambipolar diffusivity  $\eta_{AD}$  and Ohmic diffusivity  $\eta_{Ohm}$ , all in logarithmic scale, for the  $\lambda = 2.4$  Slw-MRN1<sup>R</sup> reference model at a later time  $t \approx 165.6$  kyr. The poloidal velocity field (top-left) and magnetic field (top-right) are shown as orange arrows. Length unit of the axes is in AU.

The formation and growth of the RSD in this tr-MRN model owes to the enhanced AD, which weakens the coupling of neutral gas to the magnetic field and allows the gas to collapse or rotate without dragging as much magnetic flux as in the MRN reference model. As shown in Fig. 12 at a typical time  $t \approx 148.0$  kyr, the ambipolar diffusivity  $\eta_{AD}$  along the equatorial region is generally

result, the disk mass is much larger than the stellar mass at the end of the simulation.

above  $10^{18} \text{ cm}^2 \text{ s}^{-1}$ , at least a few  $10^1$  times higher than that of the MRN reference model; this provides a sufficient gas-field decoupling for the infalling envelope material (Krasnopolsky et al. 2010). In the disk,  $\eta_{AD}$  reaches  $\geq 10^{21} \text{ cm}^2 \text{ s}^{-1}$ , even  $\sim 10$  times higher than the Ohmic diffusivity  $\eta_{Ohm}$ , consistent with the analytical result above (Fig. 2). The high ambipolar diffusivity in this tr-MRN model ensures a low influx of magnetic flux throughout the entire envelope, as shown in the middle panel of Fig. 13. Comparing the “first core” stage, the total magnetic flux inside any given radius (cylinder) is a few times smaller in the tr-MRN model than that of

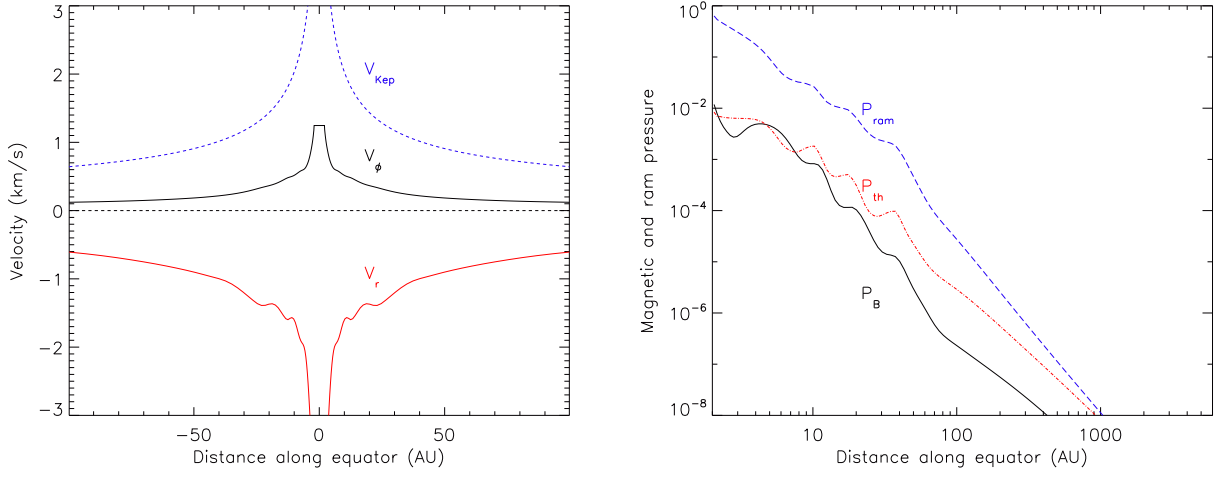


**Figure 10.** Left panel: profile of equatorial infall and rotation speed in the  $\lambda 2.4$  Slw-MRN1<sup>R</sup> reference model at  $t \approx 165.6$  kyr (same time frame as Fig. 9). The Keplerian speed is also plotted based on the central mass. Right panel: profile of thermal  $P_{\text{th}}$ , magnetic  $P_B$ , and ram  $P_{\text{ram}}$  pressures along the equator.

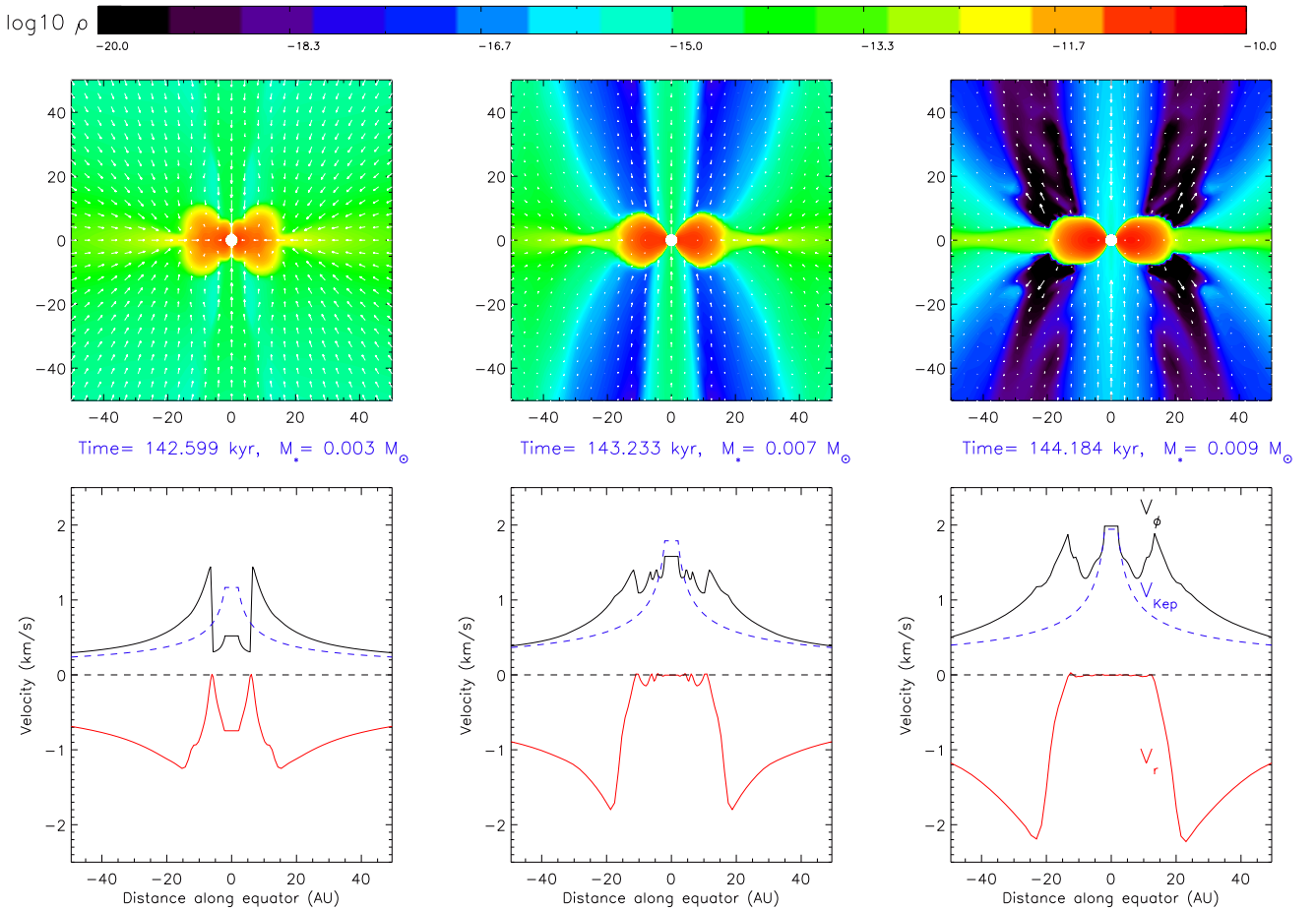


**Figure 11.** Early evolution of density distribution (color map) and velocity field (white arrows) for the  $\lambda 2.4$  Slw-trMRN1 model inside 50 AU radius. The corresponding velocity profiles along the equator are plotted in the bottom panels.

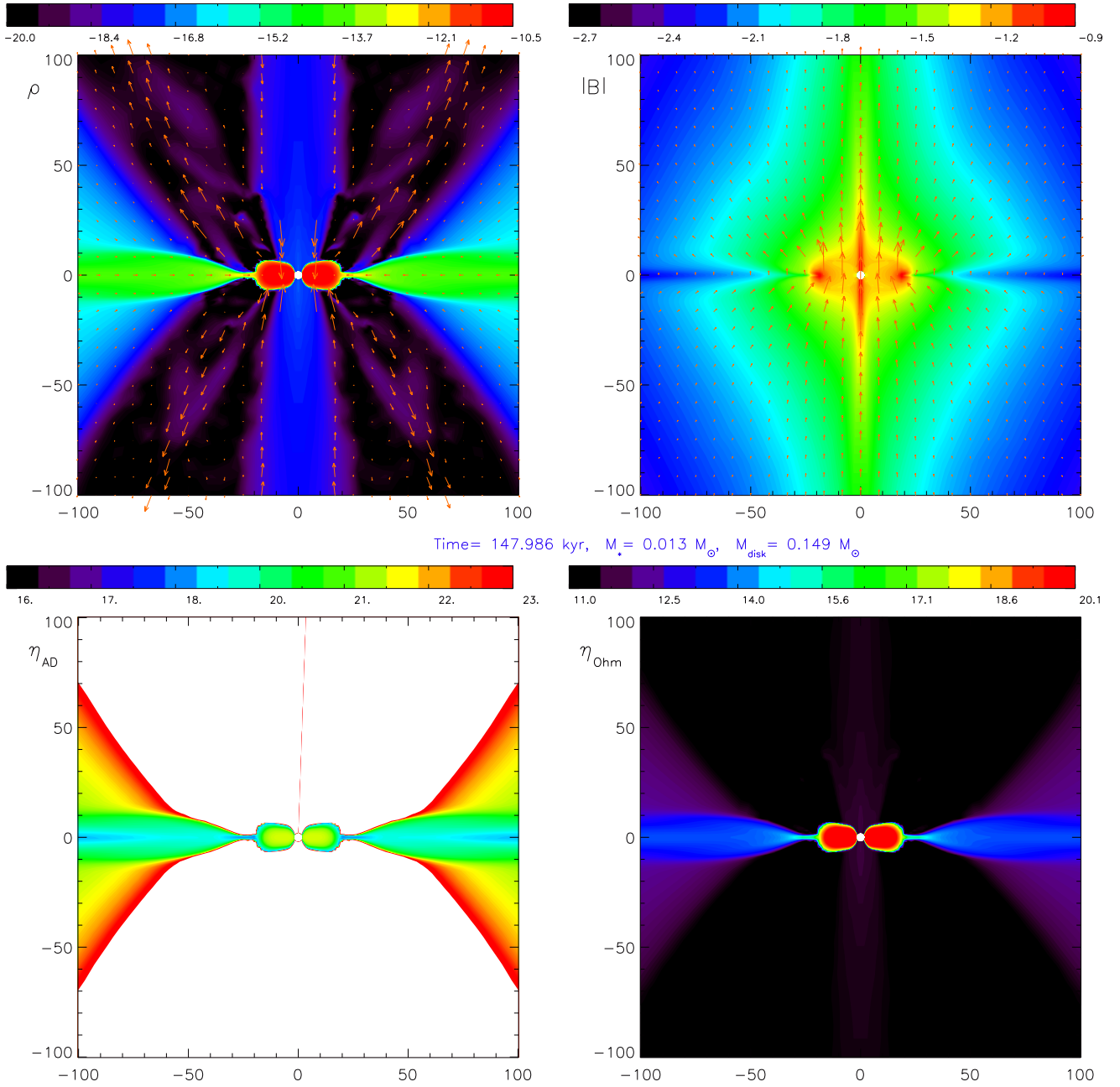


**Figure 12.** Distributions of density  $\rho$ , magnetic field strength  $|B|$ , ambipolar diffusivity  $\eta_{\text{AD}}$  and Ohmic diffusivity  $\eta_{\text{Ohm}}$ , all in logarithmic scale, for the  $\lambda = 2.4$  Slw-trMRN1 model at a later time  $t \approx 148.0$  kyr. The poloidal velocity field (top-left) and magnetic field (top-right) are shown as orange arrows. The white bipolar regions in the bottom-left panel are of high  $\eta_{\text{AD}}$  above  $10^{23} \text{ cm}^2 \text{ s}^{-1}$ . Length unit of the axes is in AU.

the MRN reference model. While having a similar total mass, the resulting mass-to-flux ratio at any given radius is also larger in the tr-MRN model by a few times.

A direct consequence of the reduced magnetic flux everywhere is a higher angular momentum in the gas, because of a weaker magnetic braking (assuming a similar magnetic field geometry). The left panel of Fig. 14 shows the specific angular momentum in each shell of gas from the inner 2 AU hole to the edge of cloud at the “first core” stage. Except for the cloud edge where collapse is still slow, gas in the tr-MRN model clearly retains higher

specific angular momentum in any given shell than the MRN reference model. This also holds over the subsequent collapse; as more materials that have experienced less magnetic braking bring in more angular momentum, a RSD is able to survive and even grow in size. Notice that there is a “plateau” near  $\geq 10\text{--}30$  AU in the tr-MRN model and  $\sim 4\text{--}10$  AU in the MRN reference model, indicating the centrifugal barrier where the free-falling gas starts to feel the centrifugal force inside. The centrifugal barrier in the MRN reference model will disappear quickly in less than 300 years as gas with low specific angular momentum keeps falling in, which again

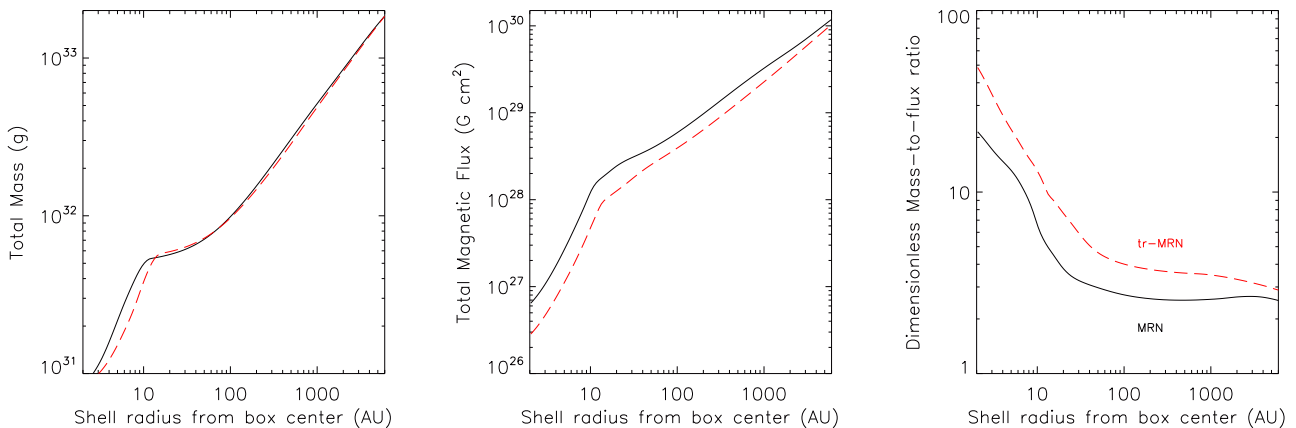


**Figure 13.** Distribution of total mass (left panel), total magnetic flux (middle panel) and the corresponding mass-to-flux ratio (right panel) inside spheres of different radii for the  $\lambda 2.4$  Slw-MRN1<sup>R</sup> reference model (black solid) at  $t \approx 165.1$  kyr and the  $\lambda 2.4$  Slw-trMRN1 model (red dashed) at  $t \approx 143.0$  kyr. The time frames are chosen at roughly the “first-core” phase when central structures are relatively simple.

implies the unsustainable nature of the small transient RSD formed in these cases. In contrast, the centrifugal barrier remains in the tr-MRN model as more angular momentum flows in with gas (not plotted). Note that the rapid decrease of specific angular momentum just inside the plateau is caused by the strong magnetic braking at this location (see the next section § 5.2.c for detailed analysis).

The location of centrifugal barrier, i.e. centrifugal radius  $R_{\text{cent}}(r_{\text{sh}})$  for gas in any give shell  $r_{\text{sh}}$ , can be approximated by the following formula,

$$R_{\text{cent}}(r_{\text{sh}}) = \frac{j(r_{\text{sh}})^2}{G(M_* + \int_{r < r_{\text{sh}}} M(r))}, \quad (26)$$

where  $M_*$  is the star mass and  $j(r_{\text{sh}})$  is the averaged specific angular momentum in this shell; and we assume all the mass interior to this shell collapses self-similarly towards the origin, hence contributing to the gravitational force for this shell. The formula is only an approximation, in which we ignore the persistent magnetic braking during collapse, and the non-spherical distribution of mass in the circumstellar region, especially the bipolar outflow which will decrease the mass inside  $r_{\text{sh}}$ .

The distribution of centrifugal radii for the “first core” stage is shown in the right panel of Fig. 14. The tr-MRN model has a much larger centrifugal radius for each given shell than the MRN reference model, consistent with the dependence on the square of specific angular momentum,  $j^2$ . In the tr-MRN model, circumstellar materials in a few  $10^1$  to a few  $10^2$  AU are expected to settle down at a centrifugal radius of  $\sim 8$ – $20$  AU; while materials in a similar region in the MRN reference model are likely to land within a few AU radius or even enter the inner 2 AU hole (considered as accreted by the star). These expectations are indeed realized at later times, when the disk in the tr-MRN model reaches a radius of  $\sim 15$ – $20$  AU and the MRN reference model shows no disk at all. Therefore, the centrifugal radius  $R_{\text{cent}}(r_{\text{sh}})$  estimated from Eq. 26 is a good indicator of the expected disk size. It reinforces the notion that a long-lived RSD with a reasonable size requires continuous supply of high angular momentum materials from the envelope, which have reasonably large centrifugal radii.

### 5.2.c Centrifugal Shock and Magnetic Braking

The presence of a centrifugal barrier naturally creates a shock by slowing down and piling up infalling materials. As a result, magnetic field geometry changes abruptly from 1) pinched field lines outside centrifugal radius — dragged by rapid accretion flow onto the disk — to 2) straight vertical field lines inside the centrifugal radius where infall motions are largely halted. At the centrifugal radius where the field lines pile up, magnetic pressure strengthens, and magnetic braking becomes efficient (see below). The centrifugal radius is also the launching site of the outflow via the magneto-centrifugal acceleration (“slingshot”) mechanism (Blandford & Payne 1982; Pudritz & Norman 1986). Note that part of the outflow region is affected by the force limiter technique.

We present in Fig. 15 the typical centrifugal shock formed in model  $\lambda 2.4$  Slw1-trMRN at a representative time  $t \approx 148.0$  kyr. The centrifugal barrier locates near the disk outer edge at  $\sim 20$  AU from the central star, where gas density is high and magnetic field strengthens to  $\sim 0.1$  G (Fig. 12). In the pre-shock region ( $\geq 20$  AU), there is a rapid increase in magnetic pressure  $P_B$  and a corresponding drop in the infall ram pressure  $P_{\text{ram}}$ . The rotational velocity  $v_\phi$  also rises quickly as the free-falling gas starts to become centrifugally supported and spins up when moving to smaller radii. In the post-shock region ( $\leq 15$  AU), gas infall motion along the equator halts almost completely ( $v_r \rightarrow 0$ ), leading to the drastic decrease in ram pressure. It implies that the disk gas has high enough angular momentum to orbit without falling further inward. The lower rotation speed in the middle section of the disk is simply because of the small total mass and gravitational potential inside. In the innermost 6 AU where gravity is mainly dominated by the central star, gas is able to rotate with its supposed Keplerian speed again. Notice that the post-shock region is dominated by thermal pressure, and magnetic pressure flattens to  $\sim 10^{-4}$  g cm<sup>-1</sup> s<sup>-2</sup>; hence the plasma  $\beta$  can reach values above 1000.

The abrupt change of magnetic field geometry across the centrifugal radius causes a very large difference in magnetic braking efficiency. We now show that the straight field lines inside the centrifugal radius leads to inefficient magnetic braking, while the pinched field lines outside the centrifugal radius leads to very strong braking. The strength of magnetic braking can be quantified

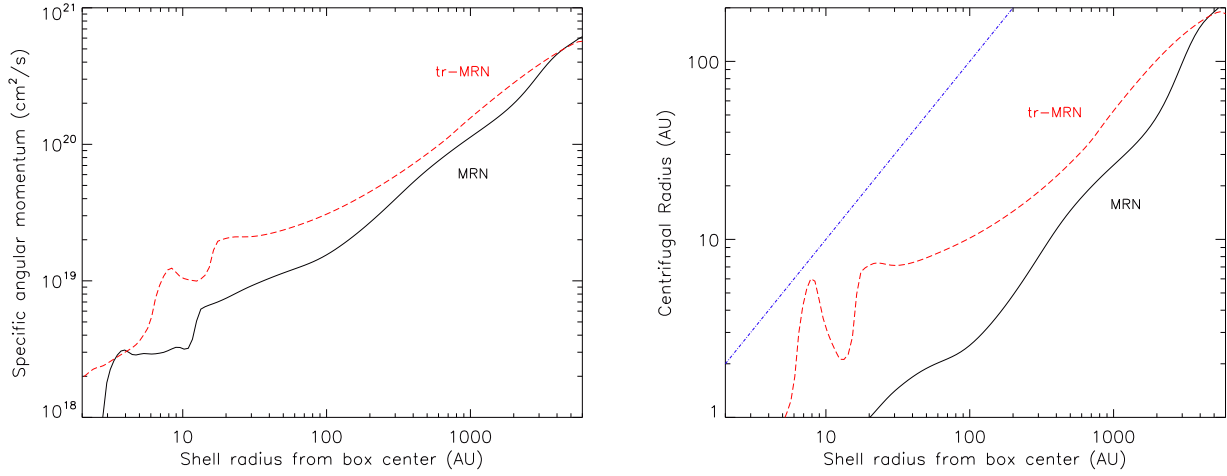


**Figure 14.** Left panel: distribution of specific angular momentum inside shells at different radii for the  $\lambda 2.4$  Slw-MRN1<sup>R</sup> reference model at  $t \approx 165.1$  kyr (black solid) and the  $\lambda 2.4$  Slw-trMRN1 model at  $t \approx 143.0$  kyr (red dashed). Right panel: the estimated centrifugal radius from Eq. 26 for the two models in the left panel. Blue dash-dotted line represents a “break-even” relation  $R_{\text{cent}}(r_{\text{sh}}) = r_{\text{sh}}$ .

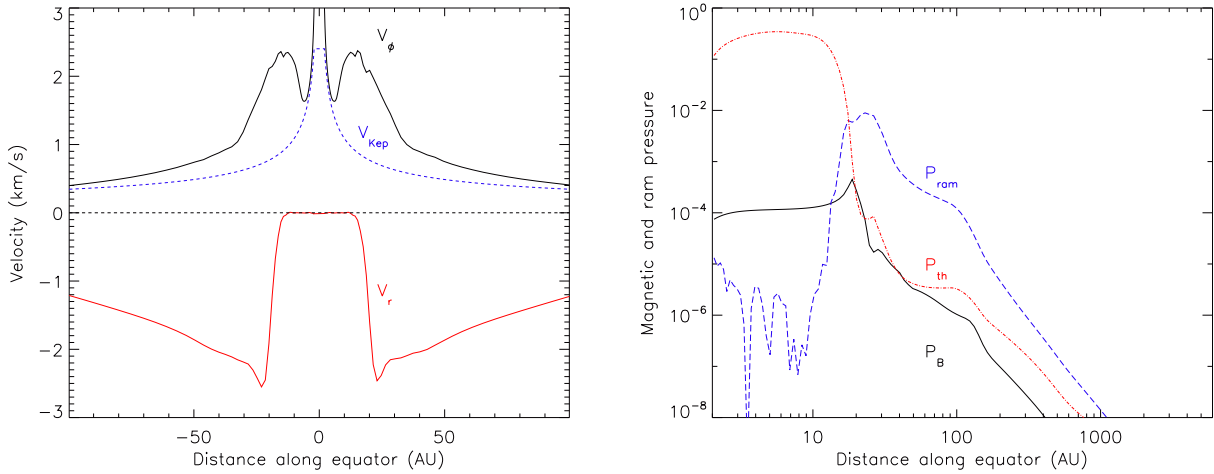


**Figure 15.** Left panel: profile of equatorial infall and rotation speed in the  $\lambda 2.4$  Slw-trMRN1 model at  $t \approx 148.0$  kyr (same time frame as Fig. 12). The Keplerian speed is also plotted based on the central mass. Right panel: profile of thermal  $P_{\text{th}}$ , magnetic  $P_{\text{B}}$ , and ram  $P_{\text{ram}}$  pressures along the equator.

by the magnetic torque integrated over a finite volume  $V$ ,

$$\mathcal{N}_m(V) = \frac{1}{4\pi} \int_V \{ \mathbf{r} \times [(\nabla \times \mathbf{B}) \times \mathbf{B}] \} dV. \quad (27)$$

Typically, the magnetic torque comes mainly from magnetic tension force rather than magnetic pressure force (the latter requires a magnetic pressure gradient in the azimuthal direction, which is zero in an axisymmetric simulation). Thus, we consider only the magnetic tension term which can be simplified to a surface integral (Matsumoto & Tomisaka 2004),

$$\mathcal{N}_t(S) = \frac{1}{4\pi} \int_S (\mathbf{r} \times \mathbf{B})(\mathbf{B} \cdot d\mathbf{S}), \quad (28)$$

over the surface  $\mathbf{S}$  of volume  $V$ . For a spherical shell at given radius  $r_{\text{sh}}$ , the net magnetic torque  $\mathcal{N}_t(r_{\text{sh}})$  exerting on it equals the difference between the two integrals over its outer and inner surfaces ( $S_{\text{out}}$  and  $S_{\text{in}}$ ),

$$\Delta \mathcal{N}_t(r_{\text{sh}}) = \mathcal{N}_t(S_{\text{out}}) - \mathcal{N}_t(S_{\text{in}}). \quad (29)$$

Therefore, the timescale to magnetically torque down the total angular momentum in this shell  $\mathcal{L}(r_{\text{sh}})$  can be estimated as,

$$t_{\text{brake}}(r_{\text{sh}}) \approx \frac{\mathcal{L}(r_{\text{sh}})}{\Delta \mathcal{N}_t(r_{\text{sh}})} \quad (30)$$

which directly measures the magnetic braking efficiency in that shell.

Fig. 16 shows the distribution of magnetic braking timescale  $t_{\text{brake}}$  for shells at different radii, in the  $\lambda 2.4$  Slw-trMRN1 model at  $t \approx 148.0$  kyr. The braking timescale is the shortest just outside the centrifugal radius  $\sim 20$  AU, with  $t_{\text{brake}} \approx 100$  years that is about 1/2 of the orbital period at that location. The strong magnetic braking matches with the field geometry outside the centrifugal radius, where strongly pinched field lines are piled up. In contrast, the braking timescale is as high as  $10^5$  years inside the disk, guaranteeing  $\sim 1000$  orbits for materials on the disk. It is a direct outcome of the straight field lines inside the centrifugal radius because

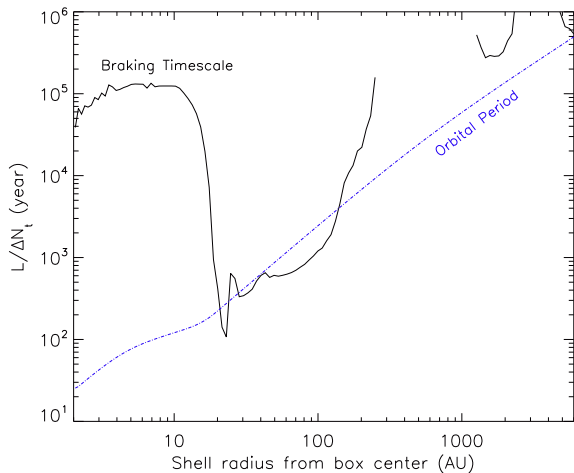


**Figure 16.** Estimated magnetic braking timescale for model  $\lambda 2.4$  Slw-trMRN1 at  $t \approx 148.0$  kyr. The orbital timescale is derived from the centrifugal velocity originated by all mass inside the given shell radius, different than that derived from stellar mass alone (Keplerian) by a factor of a few. The gap at few  $10^2$  AU indicates that magnetic torque there is transporting angular momentum inward instead of outward.

magnetic torque  $N_r$  is  $\propto B_r B_\phi$  and  $B_r \rightarrow 0$  due to negligible infall motion.

We expect in 3D a larger infall motion along the disk due to gravitational and possibly MHD instabilities, which would slightly pinch magnetic field lines again inside the centrifugal radius. However, the general result should still hold because of the large ambipolar diffusivity in the disk, which will greatly weaken the magnetic braking effect even when the field lines are pinched and winded-up slightly (Krasnopolsky et al. 2010).

### 5.3 Compound Disk: Effect of Initial Rotation and Magnetic Field

We now investigate the RSDs formed in models with faster initial rotation ( $\lambda 2.4$  Fst-trMRN1) and/or weaker initial magnetic field ( $\lambda 4.8$  Fst-trMRN1); both help the formation of RSDs by increasing the amount of angular momentum in circumstellar region. The two models  $\lambda 2.4$  Fst-trMRN1 and  $\lambda 4.8$  Fst-trMRN1 demonstrate formation of a “compound disk” consisting a small inner disk (ID) and a more massive outer ring (OR). The compound disk is an evolutionary outcome of a large single disk ( $\gtrsim 30$  AU) that forms first and separates into the two substructures (ID and OR). The separation is mainly caused by the competition of gravitational potential at the origin and that near the massive centrifugal barrier. Gas in the disk middle section feels the least gravitational force; therefore it either falls towards the origin or it is pulled backward by the mass accumulated near the centrifugal barrier depending on its location. Gradually, a gap opens up in the disk middle section, which separates the single disk into ID and OR;<sup>5</sup> both are rotationally sup-

<sup>5</sup> For the previous model  $\lambda 2.4$  Slw-trMRN1 with slower rotation and stronger magnetic field, the single disk does not separate into a “compound disk” because the centrifugal radius is small, so that the gravitational potential peaked at the centrifugal barrier is not well separated from the primary gravitational potential at the origin.

ported. For a much wider gap in model  $\lambda = 4.8$  Fst-trMRN1, the ID can eventually disappear, leaving only a massive self-gravitating OR across the centrifugal barrier.

#### 5.3.a Effect of Faster Initial Rotation

Fig. 17 shows the early evolution of the RSD formed in model  $\lambda 2.4$  Fst-trMRN1. Within 3.5 kyr after the “first core” stage, the disk grows quickly from  $\sim 15$  AU to  $\sim 35$  AU — twice of the disk size in model  $\lambda 2.4$  Slw-trMRN1 — owing to the higher specific angular momentum of infalling gas in this faster rotating core. The growth of disk size indicates that envelope materials at larger radii have larger centrifugal radii (solid-body rotation profile). The rotation motion along the equatorial region is also well above Keplerian throughout the evolution, except for the disk middle section (few AU size) where cancellation of gravitational force occurs.

The compound disk for model  $\lambda 2.4$  Fst-trMRN1 is clearly presented in Fig. 18 at a later time  $t \approx 230.4$  kyr. The whole disk is roughly twice the size of that in the slower rotating Slw-trMRN1 model. The small inner disk (ID) has a radius of  $\sim 5$  AU and the outer ring (OR) extends from 20 AU to 40 AU. The total mass of compound disk is about  $\sim 0.317 M_\odot$  at this time, with around  $\sim 95\%$  of mass in the OR. Such a massive ring in 3D will become gravitationally unstable, driving spiral waves that would redistribute angular momentum, as well as potentially fragmenting into companion objects. In contrast, the stellar mass is only  $\sim 0.031 M_\odot$ , 10% of the whole compound disk, but still twice of the ID mass. Again, we expect in 3D the mass ratio of star to disk be higher as a result of efficient gravitational instability in the disk which promotes infall towards the star.

The centrifugal shock locates at  $\sim 35$ –40 AU away from the center. Magnetic field lines are pinched outside the centrifugal radius but straighten up inside. Across the centrifugal shock, magnetic field lines pile up and field strength enhances to  $\sim 0.015$  G. The values of ambipolar and Ohmic diffusivity along the equatorial region are similar to those in the Slw-trMRN1 model. In both ID and OR, diffusivities are high, and AD dominates over Ohmic dissipation. The strong AD in ID and OR, as well as an inefficient magnetic braking there due to straight field lines, helps gas to maintain a super-Keplerian rotation (Fig. 19). The disk gap is rotating slightly slower than Keplerian speed; yet it is doing so in the positive direction, which results from a competition between thermal pressure gradient and gravitational force (not shown). Besides, both ID and OR are dominated by thermal pressure, with plasma  $\beta$  of few  $10^3$  up to  $10^4$ .

#### 5.3.b Effect of Weaker Initial B-field

We investigate the effect of initial magnetization by comparing model  $\lambda 4.8$  Fst-trMRN1 to the previous model  $\lambda 2.4$  Fst-trMRN1. A weaker magnetic field results in a lower total magnetic flux. We again compare the “first core” stage for the two models, when structures in the central region are relatively simple. As shown in middle panel of Fig. 20, the magnetic flux in  $\lambda = 4.8$  model is about half of that in the  $\lambda = 2.4$  model almost everywhere. The high magnetic flux in the  $\lambda = 4.8$  model between  $\sim 50$ –200 AU owes to the large amount of mass piled up at the centrifugal barrier (left panel). Nevertheless, the resulting mass-to-flux ratio clearly shows the  $\sim 2$  times difference between the two models (right panel) at all radii.

The reduced magnetic flux and higher mass-to-flux ratio in the  $\lambda = 4.8$  model enable the infalling gas to retain even more angular momentum. The angular momentum on the  $\sim 50$  AU scale is so

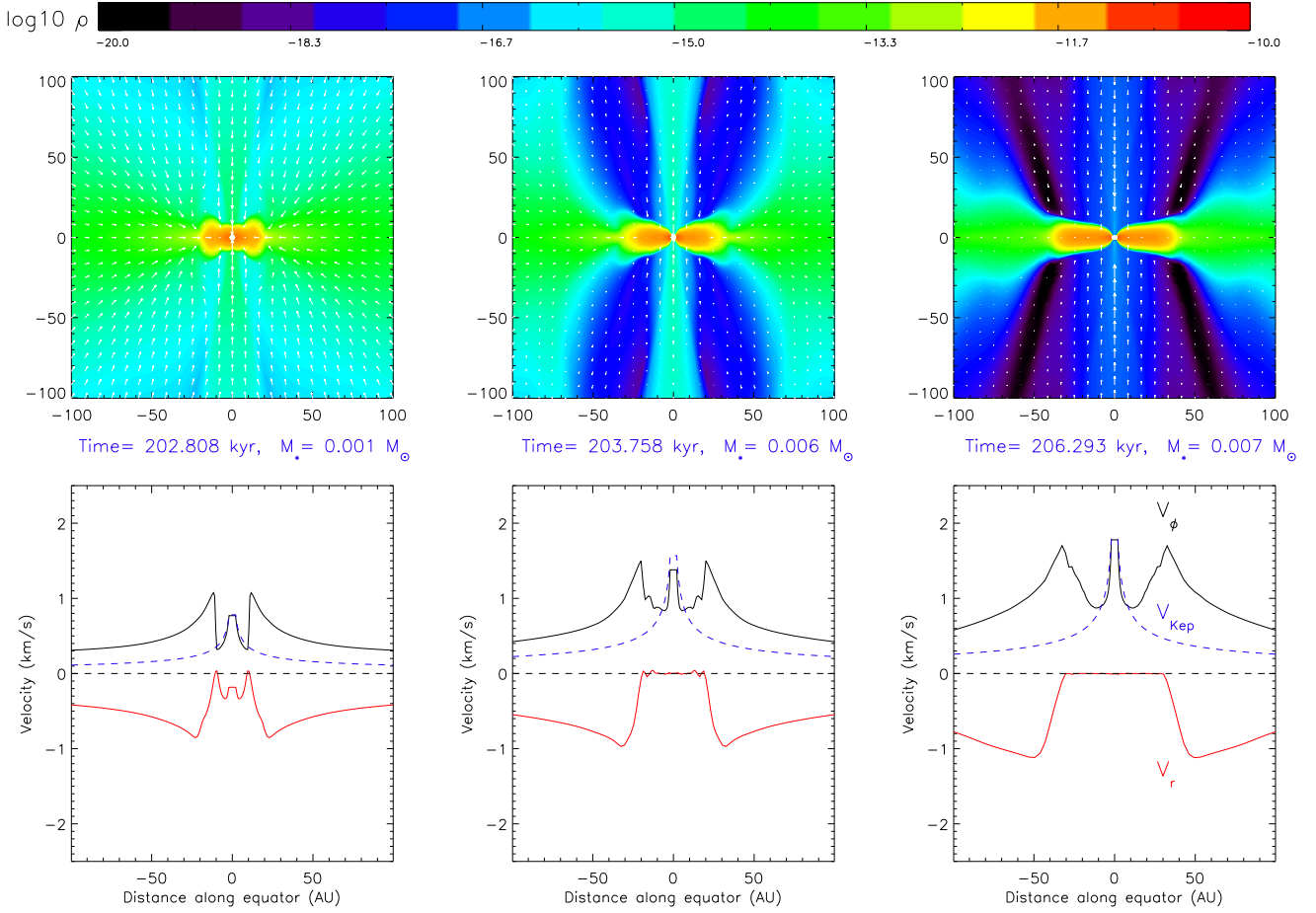


**Figure 17.** Early evolution of density distribution (color map) and velocity field (white arrows) for the  $\lambda 2.4$  Fst-trMRN1 model inside 100 AU radius. The corresponding velocity profiles along the equator are plotted in the bottom panels.

high that little matter reaches closer to the center, leaving the specific angular momentum there paradoxically lower than that of the stronger field case (left panel of Fig. 21). This is consistent with the delay in mass inflow shown in Fig. 20. The “plateau” on the specific angular momentum curve again indicates the current centrifugal barrier. Difference in specific angular momentum is the largest near the plateau, where the  $\lambda = 4.8$  curve is 2–3 times higher than the  $\lambda = 2.4$  curve. We can also estimate the expected centrifugal radius for gas in any given shell from Eq. 26, plotted in the right panel of Fig. 21. In the  $\lambda = 2.4$  model, circumstellar gas between  $\sim 25$ – $200$  AU are likely to land within  $\sim 20$ – $50$  AU; while the bulk of envelope gas in the  $\lambda = 4.8$  model are expected to gather beyond  $\geq 70$  AU. Furthermore, part of the  $\lambda = 4.8$  curve even runs above the “break-even” line  $R_{\text{cent}}(r_{\text{sh}}) = r_{\text{sh}}$  at  $\sim 40$ – $80$  AU, predicting that materials in these locations will move outward instead of falling in, because the total mass inside is unable to hold the current orbits of these materials. The large centrifugal radius in the  $\lambda = 4.8$  model, though an approximation, is direct evidence of high angular momentum in the infalling gas; it again implies weak magnetic braking as a result of the reduced magnetic flux.

The compound disk in this weaker field model ( $\lambda 4.8$  Fst-trMRN1) loses its ID as evolution continues, leaving only the massive OR located at  $\sim 35$ – $60$  AU away from the central star. In Fig. 22, we present a representative moment at  $t \approx 180.0$  kyr,

about 7 kyrs before the ID’s disappearance. At the moment, the total mass of compound disk is  $\sim 0.201 M_{\odot}$ , with  $\sim 98.7\%$  of mass in the OR. However, the central star only has  $\sim 0.008 M_{\odot}$ , about 4% of the compound disk. Even adding up the mass of star and ID ( $0.0026 M_{\odot}$ ), the central part only weighs 5.5% of the OR. Therefore, the massive self-gravitating OR not only will likely fragment as in the previous model, but indeed dominates the gravitational potential in circumstellar region. Materials in between the star and OR are more likely to fall back towards the OR, as the OR builds up more mass from the collapsing envelope.

The backward accretion onto the OR is more clearly demonstrated in Fig. 23. Materials in the disk gap between  $\sim 15$ – $35$  AU gain positive  $v_r$  and negative  $v_{\phi}$ , which indicates they are moving outward and rotating backwardly around the OR! In this weaker field model, gravitational and non-magnetic effects dominate the disk dynamics. Magnetic effects are only strong outside the centrifugal radius at  $\sim 60$ – $70$  AU, where field lines are pinched and field strength is enhanced (to less than 10 mG). Inside both ID and OR, ambipolar and Ohmic diffusivities are high; and thermal pressure again dominates which results in a plasma  $\beta$  of several  $10^3$ .

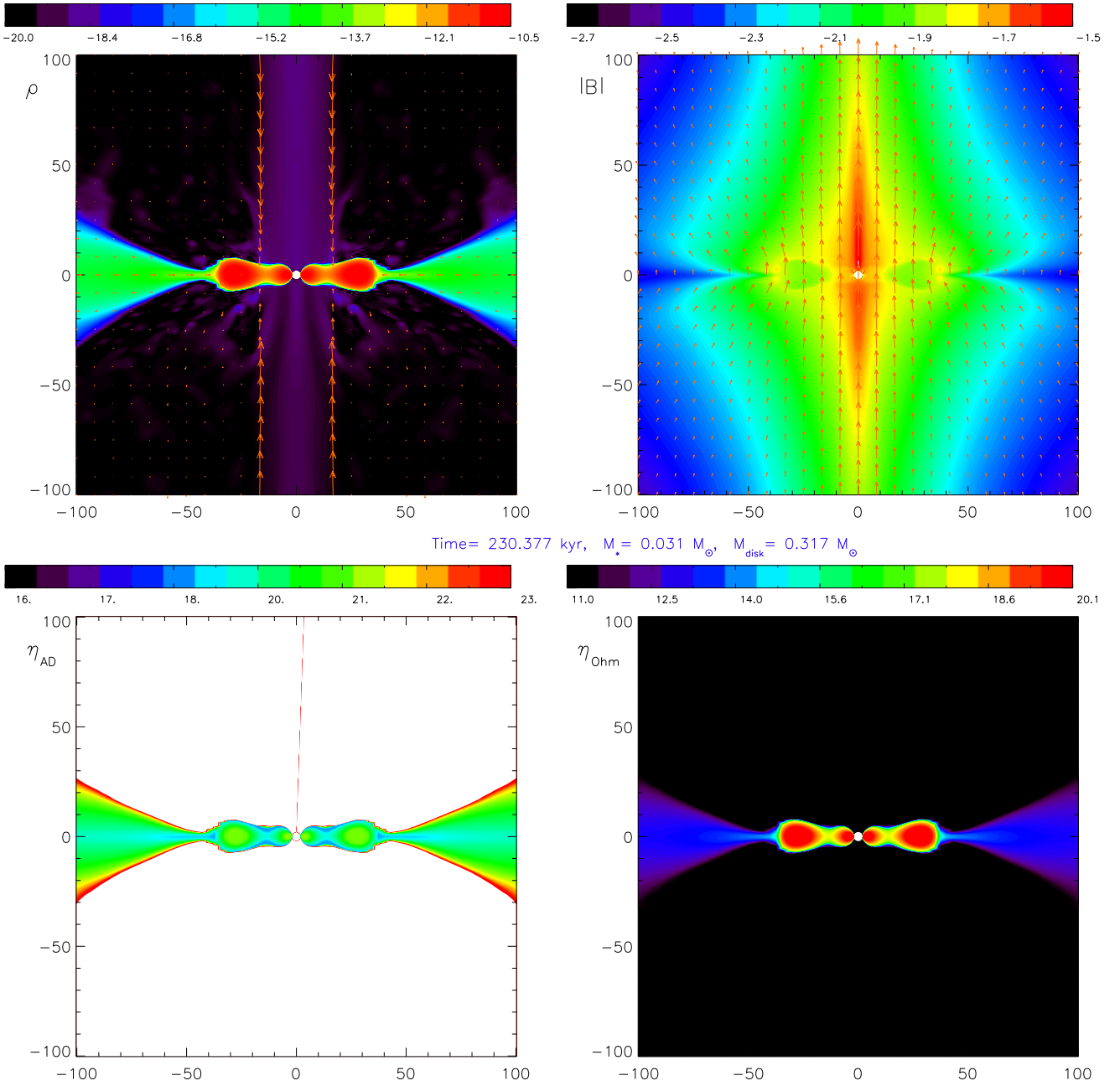


**Figure 18.** Distributions of density  $\rho$ , magnetic field strength  $|B|$ , ambipolar diffusivity  $\eta_{AD}$  and Ohmic diffusivity  $\eta_{Ohm}$ , all in logarithmic scale, for the  $\lambda = 2.4$  Fst-trMRN1 model at a later time  $t \approx 230.4$  kyr. The poloidal velocity field (top-left) and magnetic field (top-right) are shown as orange arrows. The white bipolar regions in the bottom-left panel are of high  $\eta_{AD}$  above  $10^{23} \text{ cm}^2 \text{ s}^{-1}$ . Length unit of the axes is in AU.

#### 5.4 Shrinking Disk, LG models, and Cosmic-Ray Ionization Rate

Finally, we briefly describe the type (ii) shrinking disk formed in our simulations. This type of disks mainly form in models with fast initial rotation and/or weaker initial B-field, but the other two key parameters being more demanding (e.g., MRN or LG grain, or high  $\zeta_0^{H_2}$ ). RSDs do appear in early times because the fast rotating materials have not yet been torqued down by magnetic braking; they even grow in size early on, depending on the angular momentum

reservoir in the circumstellar region in different models. However, because of a low ambipolar diffusivity in the low density envelope, large amount of magnetic flux is being dragged by the collapsing flow into the high density circumstellar region. The direct consequence is a strong magnetic braking as soon as field lines become pinched along the equator. Therefore, when gas eventually lands onto the disk, it supplies less specific angular momentum to the disk than what is required to sustain the disk rotation. Gradually, these RSDs shrink in size, and some may disappear in about  $10^4$  years (see Table 1–2). Therefore, it is the strong magnetic braking

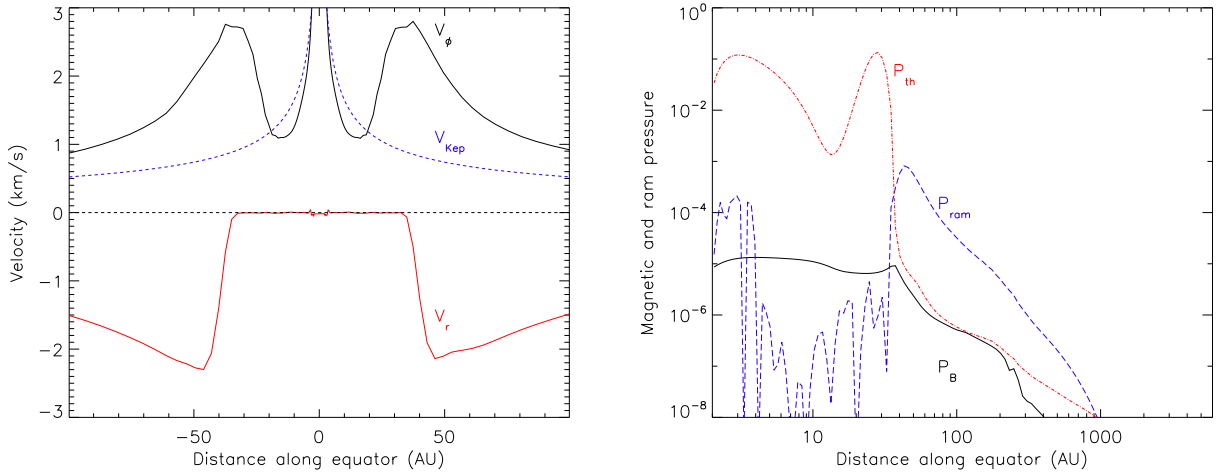


**Figure 19.** Left panel: profile of equatorial infall and rotation speed in the  $\lambda 2.4$  Fst-trMRN1 model at  $t \approx 230.4$  kyr (same time frame as Fig. 18). The Keplerian speed is also plotted based on the central mass. Right panel: profile of thermal  $P_{th}$ , magnetic  $P_B$ , and ram  $P_{ram}$  pressures along the equator.

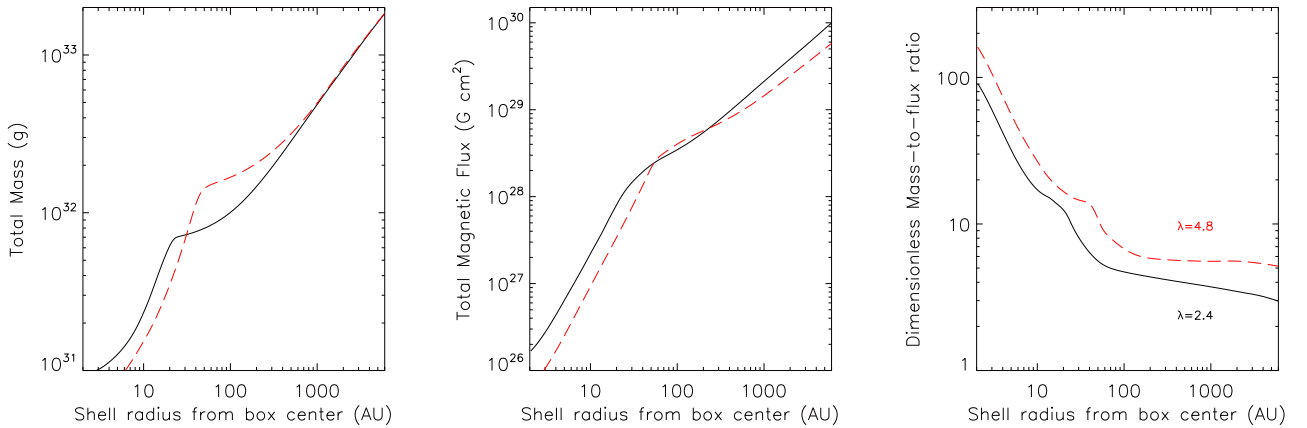


**Figure 20.** Distribution of total mass (left panel), total magnetic flux (middle panel) and the corresponding mass-to-flux ratio (right panel) inside spheres of different radii for the strong field model  $\lambda 2.4$  Fst-trMRN1 (black solid) at  $t \approx 203.1$  kyr and the weak field model  $\lambda 4.8$  Fst-trMRN1 (red dashed) at  $t \approx 164.8$  kyr. The time frames are chosen at roughly the “first-core” phase when physical structures are relatively simple.

and insufficient angular momentum influx that fail to maintain a long-lived reasonably sized RSD.

We take model  $\lambda 4.8$  Fst-MRN1 for example. Fig. 24 shows the evolution of the shrinking disk. The disk radius shrinks roughly by 40%, from 25 AU to 15 AU over a period of 3.8 kyrs, and will continue to shrink for another 3 kyrs to a radius of 10AU. Unlike other models discussed above, the later phases of this model (middle and right panels) show a rapid decrease in rotation speed  $v_\phi$  along the flattened pseudo-disk close to the disk edge (centrifugal barrier). At time 168.6 kyr (right panel) in particular,  $v_\phi$  has reduced to  $\sim 0$  between 15–20 AU. It is a direct outcome of strong magnetic braking outside the centrifugal radius, where magnetic field lines are strongly pinched and piled up, as discussed in § 5.2.c. Besides, there is a plateau in the infall speed just outside the centrifugal barrier (between 10–15 AU), which is also a typical feature of the “re-summed” infall motion for magnetically braked materials (Li et al.

2011). Note that the infall motion still halts in the innermost  $\sim 7$  AU inside the centrifugal barrier.

The efficient magnetic braking outside the centrifugal radius is shown more clearly in Fig. 25, in which we plot the distribution of magnetic braking timescale  $t_{brake}$  (Eq. 30) for the middle panel of Fig. 24 ( $t \approx 166.7$  kyr). Over a wide circumstellar region between 20–100 AU, the braking timescale is already as short as a fraction of the estimated orbital period; it reaches a minimum value of  $\sim 10^2$  years just outside the centrifugal radius at  $\sim 20$  AU. At such location, the loss of angular momentum via magnetic braking takes only  $1/4$ – $1/3$  orbits, more efficient than the  $\lambda 2.4$  Slw-trMRN1 model discussed above (Fig. 16).

The strong magnetic braking essentially results from a large amount of magnetic flux that has brought into the circumstellar region by the collapsing flow. AD in this model ( $\lambda 4.8$  Fst-MRN1) is rather inefficient throughout the envelope because of the MRN grains. In contrast, the model  $\lambda 2.4$  Slw-trMRN1 discussed

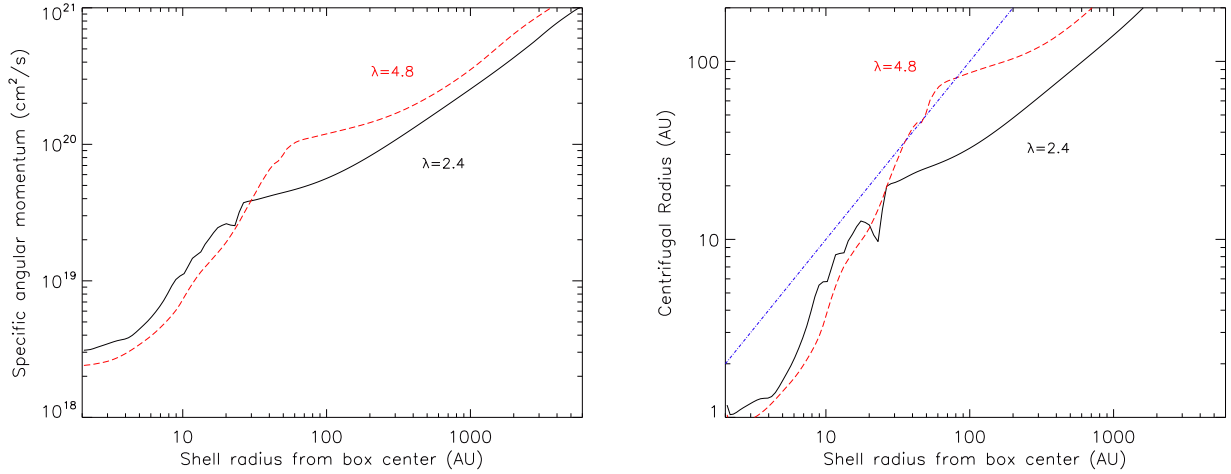


**Figure 21.** Left panel: distribution of specific angular momentum inside shells at different radii for the strong field model  $\lambda 2.4$  Fst-trMRN1 at  $t \approx 203.1$  kyr (black solid) and the weak field model  $\lambda 4.8$  Fst-trMRN1 at  $t \approx 164.8$  kyr (red dashed). Right panel: the estimated centrifugal radius from Eq. 26 for the two models in the left panel. Blue dash-dotted line represents a “break-even” relation  $R_{\text{cent}}(r_{\text{sh}}) = r_{\text{sh}}$ .

in § 5.2.b, though starting with a disadvantage in the initial magnetic field strength (stronger) and rotation speed (slower), has much more efficient AD to help decouple infalling gas from the magnetic field because of the tr-MRN grains. As a result, less magnetic flux has reached the circumstellar region 20–100 AU than in the  $\lambda 4.8$  Fst-MRN1 model at a similar evolution stage (Fig. 26). Because the magnetic field lines are strongly pinched along the equatorial region outside the centrifugal radius, the larger magnetic flux in model  $\lambda 4.8$  Fst-MRN1 hence yields stronger magnetic braking in such region. This is the origin for the shrinkage of the disk.

Shrinking RSDs are also formed in LG models with low cosmic-ray ionization rate; faster rotation and/or weaker magnetic field helps as well (see Table 1-2). The performance of LG models in terms of disk formation largely resembles that of the MRN models, yet is slightly better in terms of disk lifetime and size. This is expected from the analytical result above (Fig. 2). Compared to the MRN case, the LG case has a larger AD diffusivity by  $\sim 1$  order of magnitude at low densities ( $\lesssim 10^9$  cm $^{-3}$ ), which enables more angular momentum to be retained in the rotating envelope; however, such angular momentum surplus is mostly removed by a stronger magnetic braking along the equatorial region, because the AD diffusivity at high densities ( $\gtrsim 10^9$  cm $^{-3}$ ) in the LG case is indeed lower by a factor of few than that in the MRN case. Therefore, LG models can form larger disks than MRN models due to larger centrifugal radius of envelope gas. However, the weaker AD along the equatorial region leads to a stronger magnetic braking, so that these RSDs still shrink over time.

Although the effect of cosmic-ray ionization rate is not the main focus of this study, we rank it as the second most important parameter for formation of RSDs after the grain size distribution. When we increase  $\zeta_0^{\text{H}_2}$  to  $5.0 \times 10^{-17}$  s $^{-1}$ , most of long-lived RSDs (Y or Y $^{\text{Shrink}}$ ) formed in  $\zeta_0^{\text{H}_2} = 1.0 \times 10^{-17}$  s $^{-1}$  either become shrinking disks or shorten their lifetime so much that can only be categorized as transient type(i) disks. Changing initial rotation or magnetization does not have such a strong effect in general. We have also tested other values of  $\zeta_0^{\text{H}_2}$ , and found that  $2.0 - 3.0 \times 10^{-17}$  s $^{-1}$  has much less destructive effect than  $5.0 \times 10^{-17}$  s $^{-1}$  in terms of forming RSDs in a wider parameter space. For instance, with  $\zeta_0^{\text{H}_2} = 2.5 \times 10^{-17}$  s $^{-1}$ , long-lived RSD of 20–30 AU can still form

when grain size sets to tr-MRN, magnetic field to  $\lambda = 2.4$ , and rotation to  $\beta = 0.1$ . This may provide clues for potentially constraining cosmic-ray ionization rate of dense cores using disk observations. We will leave the detailed discussion to future studies.

## 6 SUMMARY AND DISCUSSION

We have implemented an equilibrium chemical network to study the effect of changing grain size on magnetic diffusivities, and coupled the chemistry into 2D axisymmetric MHD simulations to revisit the formation of RSDs through non-ideal MHD effects. Our main conclusions are summarized as follows.

1. Removing VSGs ( $\sim 10$  Å to few 100 Å) from the grain size distribution can increase the ambipolar diffusivity by  $\sim 1-2$  orders of magnitude at densities below  $10^{10}$  cm $^{-3}$ , because VSGs are both well-coupled to the magnetic field and able to exert strong drag to their surrounding neutral molecules, and the large number of VSGs in the size distribution greatly increase the fluid conductivity and decrease the ambipolar diffusivity.

2. Truncating the standard MRN distribution (while keeping the dust-to-gas mass ratio at 0.01) at  $a_{\text{min}} \approx 0.1$   $\mu\text{m}$  (tr-MRN case) has the optimal effect on enhancing the ambipolar diffusivity  $\eta_{\text{AD}}$  in the low density regime. In this case, both Pedersen ( $\sigma_{\text{P}}$ ) and Hall ( $\sigma_{\text{H}}$ ) conductivities of the fluid are much smaller than that with the full MRN distribution; they together raise the  $\eta_{\text{AD}}$  by  $\sim 1-2$  orders of magnitude. However, the reduction of total grain surface area only increases the ionization fraction by a factor of a few, because the effect scales with  $\propto a_{\text{min}}^{-1}$  and is partially offset by gas-phase ion-electron recombinations. Note that when  $a_{\text{max}}$  is set to 1  $\mu\text{m}$ , the optimal  $a_{\text{min}}$  occurs at  $\approx 0.055$   $\mu\text{m}$ .

3. Pedersen conductivity  $\sigma_{\text{P}}$  is normally determined by ions; however, a large number of VSGs can dominate  $\sigma_{\text{P}}$  instead, especially when  $a_{\text{min}}$  is between  $\sim 10$  Å and  $\sim 200$  Å (0.02  $\mu\text{m}$ ). For the MRN distribution in particular, the  $\sigma_{\text{P}}(g^-)$  is over 1–2 orders of magnitude larger than the contribution of ions. For the optimal tr-MRN distribution, the  $\sigma_{\text{P}}(g^-)$  is reduced by  $\sim 10^4$  times and the total  $\sigma_{\text{P}}$  by  $\sim 1-2$  orders of magnitude than those of the MRN case.

4. Hall conductivity  $\sigma_{\text{H}}$  is generally dominated by negatively

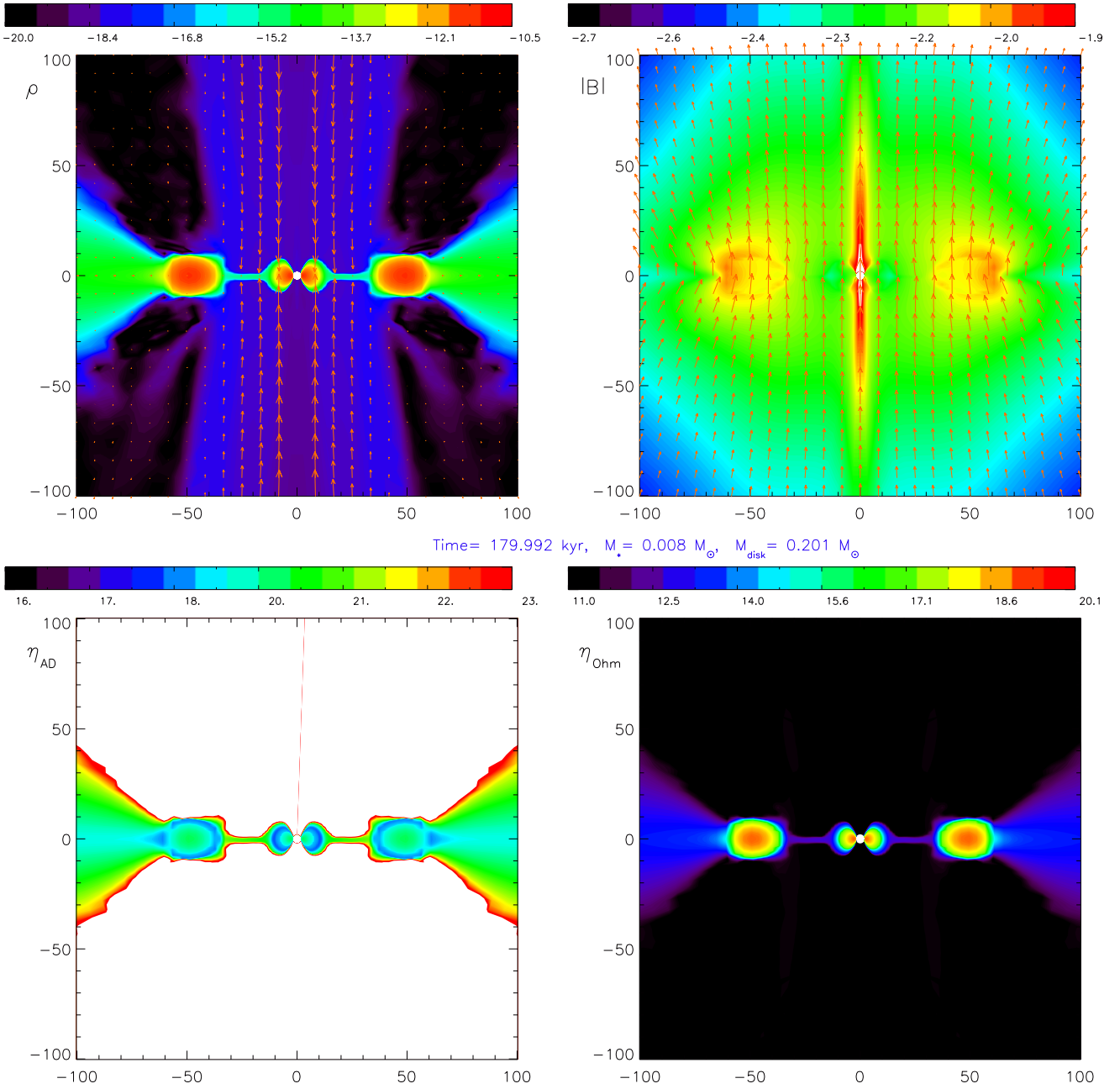


**Figure 22.** Distributions of density  $\rho$ , magnetic field strength  $|B|$ , ambipolar diffusivity  $\eta_{AD}$  and Ohmic diffusivity  $\eta_{Ohm}$ , all in logarithmic scale, for the  $\lambda = 4.8$  Fst-trMRN1 model at a later time  $t \approx 180.0$  kyr. The poloidal velocity field (top-left) and magnetic field (top-right) are shown as orange arrows. The white bipolar regions in the bottom-left panel are of high  $\eta_{AD}$  above  $10^{23} \text{ cm}^2 \text{ s}^{-1}$ . Length unit of the axes is in AU.

charged grains as long as grain size is below  $\lesssim 0.5 \mu\text{m}$  and above  $\gtrsim 10 \text{ \AA}$ . By increasing  $a_{\text{min}}$  from the MRN case to the tr-MRN case, the  $\sigma_{\text{H}}$  decreases by up to  $\sim 100$  times at densities below  $\sim 10^{10} \text{ cm}^{-3}$ , mainly because of a reduction ( $\sim 500$  times) in the fractional abundance of negatively charged grains  $x(g^-)$  and an offsetting effect from the grain's Hall parameter  $\beta_{g^-, \text{H}_2}$ . The low  $\sigma_{\text{H}}$  combines with the low  $\sigma_{\text{p}}$  in the tr-MRN case together enhances AD in the low density regime.

5. The enhanced AD by truncated MRN grains can enable massive ( $\sim \text{few } 10^{-1} M_{\odot}$ ) long-lived ( $> \text{few } 10^4\text{--}10^5$  years) RSDs to

form in 2D simulations. The efficient ambipolar diffusion of the magnetic field in the envelope reduces the amount of magnetic flux being dragged in by the collapsing flow, which weakens magnetic braking in the circumstellar region. Therefore, the infalling gas can retain enough angular momentum required for sustaining a large RSD of tens of AU.

5. Large gas angular momentum naturally leads to a large centrifugal radius that also determines the disk size. The centrifugal barrier hosts a hydrodynamic shock as infalling materials slow down and pile up. Across the shock, magnetic field geometry

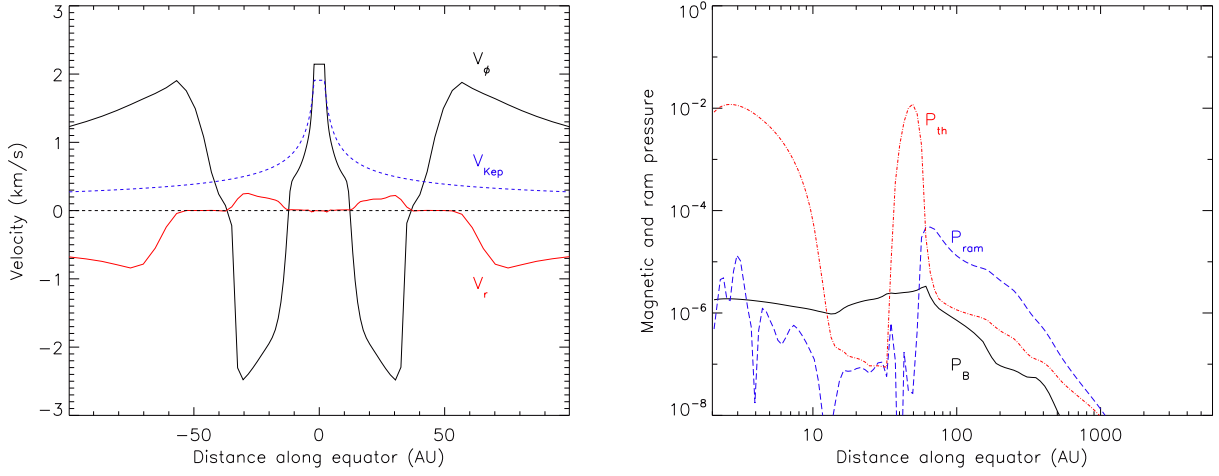


**Figure 23.** Left panel: profile of equatorial infall and rotation speed in the  $\lambda 4.8$  Fst-trMRN1 model at  $t \approx 180.0$  kyr (same time frame as Fig. 22). The Keplerian speed is also plotted based on the central mass. Right panel: profile of thermal  $P_{th}$ , magnetic  $P_B$ , and ram  $P_{ram}$  pressures along the equator.

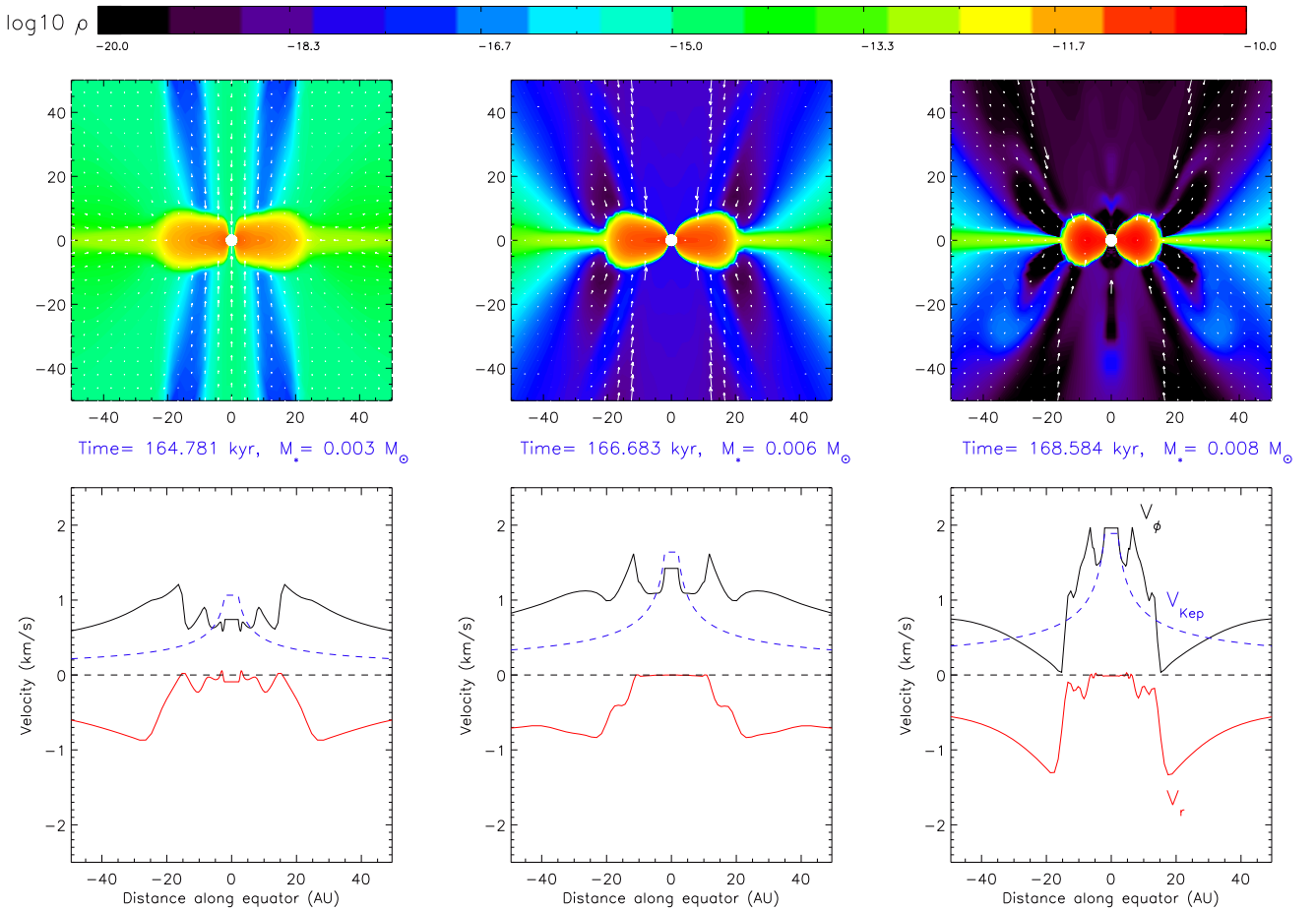


**Figure 24.** Early evolution of density distribution (color map) and velocity field (white arrows) for the  $\lambda 4.8$  Fst-MRN1 model inside 50 AU radius. The corresponding velocity profiles along the equator are plotted in the bottom panels.

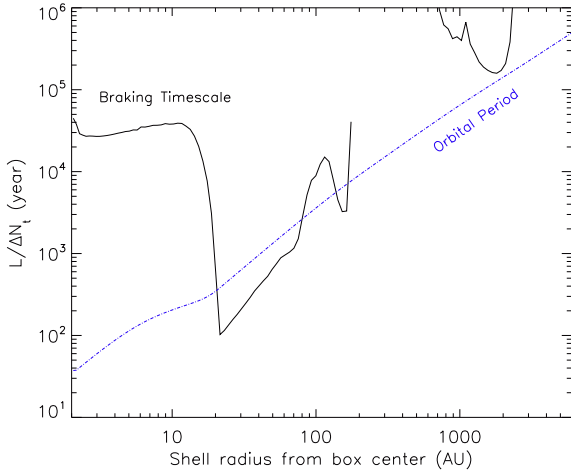


**Figure 25.** The estimated magnetic braking timescale, as in Fig. 16, but for  $\lambda 4.8$  Fst-MRN1 case at 166.7 kyr (same time frame as the middle panel of Fig. 24).

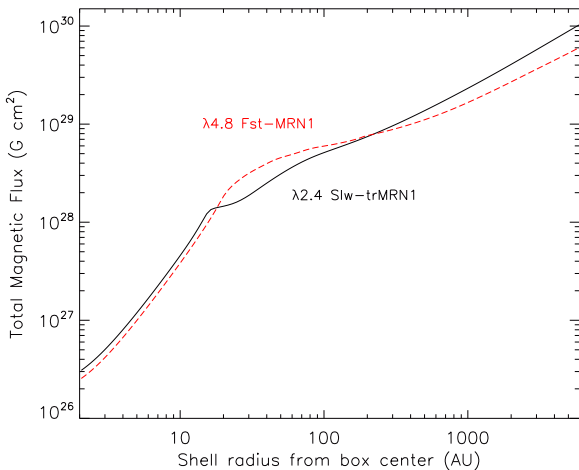


**Figure 26.** Comparison of the distribution of magnetic flux at early times for model  $\lambda 4.8$  Fst-MRN1 at 166.7 kyr (middle panel of Fig. 24) and  $\lambda 2.4$  Slw-trMRN1 at 143.2 kyr (middle panel of Fig. 11).

changes abruptly from pinched field lines outside the centrifugal radius into straight field lines inside. As a result, field lines pile up near the centrifugal radius, field strength amplifies, and magnetic braking becomes the strongest. However, inside the centrifugal radius where field lines straighten up (due to lack of infall motion), the magnetic braking timescale is much longer than the orbital period, by up to a factor of  $10^3$ .

6. Magneto-centrifugal outflows are launched at the centrifugal radius (disk edge), which, although are partly affected by the numerical technique, continuously carve the bipolar regions.

7. Faster initial rotation speed and/or weaker initial magnetic field strength further aid the formation of RSDs and increase disk size and lifetime, because of an increased amount of angular momentum available in the circumstellar region. In cases with truncated MRN grains and low cosmic-ray ionization rate, a large disk

( $\geq 30$  AU) forms first and later evolves into a “compound disk” that consists of a small Keplerian ID and a massive rotationally supported self-gravitating OR. The disk gap that separates the two substructures appears gradually as a result of competition of gravitational force from the origin and that exerted by the massive OR, i.e., gas either falls towards the origin or is pulled backward to the OR.

8. Cosmic-ray ionization rate  $\zeta^{\text{H}_2}$  also plays an important role, besides grain size, on the formation of RSDs. In order for the truncated MRN grains to avert the “magnetic braking catastrophe” and produce RSDs,  $\zeta^{\text{H}_2}$  cannot be too high. We find that  $\zeta_0^{\text{H}_2} \lesssim 2.0 - 3.0 \times 10^{-17} \text{ s}^{-1}$  on the corescale can still allow RSDs of 20–30 AU to form in strongly magnetized ( $\lambda = 2.4$ ) cores. However,  $\zeta_0^{\text{H}_2} = 5.0 \times 10^{-17} \text{ s}^{-1}$  may be too high; even when other parameters are less stringent, disk radius is at most 10–20 AU and may further shrink somewhat.

Most of the results presented here should still hold in 3D calculations. The main drawback of 2D axisymmetry is the lack of 3D gravitational and magnetic instabilities, which can redistribute angular momentum inside the disk and drive inward accretion and outward expansion (to conserve angular momentum). Therefore, in 3D, the disk would be less massive (but larger) and the star would be more massive than the ones in 2D. Disk fragmentation may also occur in 3D if massive RSDs become gravitationally unstable (Kratte et al. 2010). Hence tight binary and multiple systems with 50 AU separation or smaller may form naturally even without tightening wide binaries through magnetic braking (Zhao & Li 2013; Zhao et al. 2013). Magnetic interchange instability in the stellar vicinity has been shown to strongly hinder disk rotation and suppress disk formation, owing to the decoupled magnetic flux from accretion flow that is trapped in the circumstellar region (DEMS: decoupling-enabled magnetic structure; Zhao et al. 2011; Krasnopolsky et al. 2012). However, the DEMS is likely substantially weakened, if not eliminated, by a high AD diffusivity, which makes it difficult for the collapsing flow to drag magnetic flux close to the central object.

Although the numerical study here includes both AD and Ohmic dissipation, we have also carried out simulations with AD alone for comparison (not shown) and find the same results. The Ohmic dissipation has negligible effect on disk formation, at least within the density range and resolution limit of this study. It is easily explicable from § 4 and Fig. 2. In the MRN case, even though Ohmic diffusivity dominates over ambipolar diffusivity at high densities ( $\geq 10^{11} \text{ cm}^{-3}$ ), it has little opportunity to take effect due to a lack of dense long-lived RSD in the first place. The low AD diffusivity at low densities is simply unable to preserve enough angular momentum to sustain a well defined RSD, if any. In the tr-MRN case, Ohmic diffusivity is much smaller than ambipolar diffusivity over the entire density range in this study (even without the cap on the Ohmic diffusivity), and hence makes little difference to the result. Future studies regarding the subsequent evolution of protoplanetary disk may still consider Ohmic dissipation at a much higher density.

We have also explored different slopes of the size distribution than  $-3.5$  and found the corresponding changes on AD diffusivity are much less significant than by removing VSGs. Again, we fix the total grain mass fraction at 0.01 and  $a_{\text{max}} = 0.25 \mu\text{m}$ . When the slope is in range  $(-4.0, -3.0)$ , there is only a slight change (less than a factor of  $\sim 2$ ) to the AD curve. When the slope is in range  $(-3.0, -2.0)$ , AD diffusivity slightly enhances to the level of  $a_{\text{min}} \approx 0.035 \mu\text{m}$  in the  $-3.5$  case, which is still more than 1 order

of magnitude lower than that in the optimal  $a_{\min} \approx 0.1 \mu\text{m}$  case. Such tests, though very rough, reinforce the pivotal role of removing VSGs on enhancing the ambipolar diffusivity, which is unlikely to be replaced by a reasonable change in the slope of size distribution. We will leave the detailed analysis in a more refined chemical framework in future study.

Although grain coagulation provides natural means of removing VSGs, grain growth to  $1 \mu\text{m}$  or larger has been shown to be difficult (Hirashita & Li 2013) in dense cores unless they are relatively long lived. However, the AD enhancement discussed in this study only require moderate growth of grains. The optimal cut-off size is just around  $0.1 \mu\text{m}$  for  $a_{\max} = 0.25 \mu\text{m}$ , and around  $0.055 \mu\text{m}$  for  $a_{\max} = 1 \mu\text{m}$ . Therefore, the removal of VSGs less than few  $100 \text{ \AA}$  can be efficiently achieved in a few  $10^6$  years through grain coagulation (Rossi et al. 1991; Ossenkopf 1993; Ormel et al. 2009; Hirashita 2012). Such a process is also likely to take place during the quiescent prestellar phase which can last for several free-fall times (e.g., Ward-Thompson et al. 2007; Keto & Caselli 2010).

Another possible approach to removing VSGs from the collapsing flow is proposed by Ciolek & Mouschovias (1996); they suggest that different degrees of grain coupling to the magnetic field can cause small grains to be left behind in the low density envelope, while allow only larger grains to follow the collapse into dense part of the core. In reality, both mechanisms can operate to help removing VSGs during the prestellar and collapse phase. More complete chemistry models including advection of gas-phase and grain species as well as grain evolution are needed in non-ideal MHD simulations to obtain a more realistic picture of disk formation in particular and star formation in general. Although much work remains to be done, our calculations have strengthened the case for the non-ideal MHD effects, especially ambipolar diffusion, as a viable mechanism for enabling the formation of rotationally supported disks in even strongly magnetized cloud cores and the growth of such disks to at least tens of AUs in size.

## ACKNOWLEDGEMENTS

We thank Daniele Galli, Marco Padovani, Shu-ichiro Inutsuka, and Charles Malcolm Walmsley for inspiring discussions. BZ and PC acknowledge support from the European Research Council (ERC; project PALs 320620). Z.-Y. L. is supported in part by NASA NNX14AB38G and NSF AST-1313083. Numerical simulations are carried out on the MPG supercomputer HYDRA and our CAS group cluster at MPE.

## REFERENCES

Allen, A., Li, Z.-Y., & Shu, F. H. 2003, *ApJ*, 599, 363  
 Bergin, E. A., & Tafalla, M. 2007, *ARA&A*, 45, 339  
 Blandford, R. D., & Payne, D. G. 1982, *MNRAS*, 199, 883  
 Braiding, C. R., & Wardle, M. 2012, *MNRAS*, 422, 261  
 Cardelli, J. A., Clayton, G. C., & Mathis, J. S. 1989, *ApJ*, 345, 245  
 Caselli, P., Walmsley, C. M., Terzieva, R., & Herbst, E. 1998, *ApJ*, 499, 234  
 Caselli, P., Walmsley, C. M., Zucconi, A., Tafalla, M., Dore, L., & Myers, P. C. 2002, *ApJ*, 565, 344  
 Caselli, P., Benson, P. J., Myers, P. C., & Tafalla, M. 2002, *ApJ*, 572, 238  
 Chokshi, A., Tielens, A. G. G. M., & Hollenbach, D. 1993, *ApJ*, 407, 806  
 Ciolek, G. E., & Mouschovias, T. Ch. 1996, *ApJ*, 468, 749  
 Cleeves, L. I., Adams, F. C., Bergin, E. A. 2013, *ApJ*, 772, 5  
 Dapp, W. B., & Basu, S. 2010, *A&A*, 521, 56  
 Dapp, W. B., Basu, S., & Kunz, M. W. 2012, *A&A*, 541, 35  
 Desch, S. J., & Mouschovias, T. Ch. 2001, *ApJ*, 550, 314

Dominik, C. & Tielens, A. G. G. M. 1997, *ApJ*, 480, 647  
 Draine, B. T., & Sutin, B. 1987, *ApJ*, 320, 803  
 Forbrich, J., Lada, C. J., Lombardi, M., Román-Zúñiga, C., & Alves, J. 2015, *A&A*, 580, 114  
 Goodman, A. A., Benson, P. J., Fuller, G. A., & Myers, P. C. 1993, *ApJ*, 406, 528  
 Hasegawa, T. I., Herbst, E., & Leung, C. M. 1992, *ApJS*, 82, 167  
 Hennebelle, P., & Fromang, S. 2008, *A&A*, 477, 9  
 Hirashita, H. 2012, *MNRAS*, 422, 1263  
 Hirashita, H., & Li, Z.-Y. 2013, *MNRAS*, 434, 70  
 Joos, M., Hennebelle, P., & Ciardi, A. 2012, *A&A*, 543, 128  
 Kauffmann, J., Bertoldi, F., Bourke, T. L., Evans, N. J., II, & Lee, C. W. 2010, *A&A*, 487, 993  
 Keto, E., & Caselli, P. 2010, *MNRAS*, 402, 1625  
 Kim, S.-H., Martin, P. G., & Hendry, P. D. 1994, *ApJ*, 422, 164  
 Krasnopolsky, R., Li, Z.-Y., & Shang, H. 2010, *ApJ*, 716, 1541  
 Krasnopolsky, R., Li, Z.-Y., & Shang, H. 2012, *ApJ*, 733, 54  
 Krasnopolsky, R., Li, Z.-Y., Shang, H., & Zhao, B. 2012, *ApJ*, 757, 77  
 Kratter, K. M., Matzner, C. D., Krumholz, M. R., & Klein, R. 2010, *ApJ*, 708, 1585  
 Kunz, M., & Mouschovias, T. Ch. 2009, *ApJ*, 693, 1895  
 Kunz, M., & Mouschovias, T. Ch. 2010, *ApJ*, 408, 322  
 Larson, R. B. 1969, *MNRAS*, 145, 271  
 Li, Z.-Y., & McKee, C. F. 1996, *ApJ*, 464, 373  
 Li, Z.-Y., Krasnopolsky, R., & Shang, H. 2011, *ApJ*, 738, 180  
 Machida, M. N., & Matsumoto, T. 2011, *MNRAS*, 413, 2767  
 Masson, J., Chabrier, G., Hennebelle, P., Vaytet, N., & Commerçon, B. 2015, arXiv:1509.05630  
 Masunaga, H., & Inutsuka, S. 2000, *ApJ*, 531, 350  
 Mathis, J. S., Rumpl, W., & Nordsieck, K. H. 1977, *ApJ*, 217, 425  
 Matsumoto, T., & Tomisaka, K. 2004, *ApJ*, 616, 266  
 Masson, J., Chabrier, G., Hennebelle, P., Vaytet, N., Commerçon, B. 2015, arXiv:1509.05630  
 Mellon, R. R., & Li, Z.-Y. 2008, *ApJ*, 681, 1356  
 Mellon, R. R., & Li, Z.-Y. 2009, *ApJ*, 698, 922  
 Mestel, L., & Spitzer, L., Jr. 1956, *MNRAS*, 116, 503  
 Miller, K., & Stone, J. M. 2000, *ApJ*, 534, 398  
 McKee, C. F. 1989, *ApJ*, 345, 782  
 Mouschovias, T. Ch., & Ciolek, G. E. 1999, *ASIC*, 540, 305  
 Nakano, T., Nishi, R., & Umebayashi, T. 2002, *ApJ*, 573, 199  
 Nishi, R., Nakano, T., & Umebayashi, T. 1991, *ApJ*, 368, 181  
 Norman, C., & Heyvaerts, J. 1985, *A&A*, 147, 247  
 Oppenheimer, M., & Dalgarno, A. 1974, *ApJ*, 192, 29  
 Ormel, C. W., Paszun, D., Dominik, C., & Tielens, A. G. G. M. 2009, *A&A*, 502, 845  
 Ossenkopf, V. 1993, *A&A*, 280, 617  
 Padovani, M., Galli, D., Hennebelle, P., Commerçon, B., & Joos, M. 2014, *A&A*, 571, 33  
 Pagani L., Steinacker J., Bacmann A., Stutz A., & Henning T. 2010, *Science*, 329, 1622  
 Pinto, C., Galli, D., & Bacciotti, F. 2008, *A&A*, 484, 1  
 Pinto, C., & Galli, D. 2008, *A&A*, 484, 17  
 Pudritz, R. E., & Norman, C. A. 1986, *ApJ*, 301, 571  
 Rossi, S. C. F., Benevides-Soares, & Barbuy, B. 1991, *A&A*, 251, 587  
 Schnee, S., Mason, B., Di Francesco, J., Friesen, R., Li, D., Sadavoy, S., & Stanke, T. 2014, *MNRAS*, 444, 2303  
 Shah, M. B., Gilbody, H. B. 1982, *J. Phys. B.*, 15, 3441  
 Shu, F. H., Adams, F. C., & Lizano, S. 1987, *ARA&A*, 25, 23  
 Shu, F. H. 1991, *Physics of Astrophysics, Vol. II: Gas Dynamics* (New York: University Science Books)  
 Shu, F. H., Galli, D., Lizano, S., & Cai, M. 2006, *ApJ*, 647, 382  
 Spitzer, L., & Tomasko, M. G. 1968, *ApJ*, 152, 971  
 Steinacker J., Pagani L., Bacmann L., & Guieu S. 2010, *A&A*, 511, 9  
 Tassis, K., Willacy, K., Yorke, H. W., & Turner, N. J. 2014, *MNRAS*, 445, 56  
 Tielens, A. G. G. M., Hagen, W. 1982, *A&A*, 114, 245  
 Tobin, J. J., Hartmann, L., Chiang, H.-F., Wilner, D. J., Looney, L. W., Loinard, L., Calvet, N., & D'Alessio, P. 2012, *Nature*, 492, 83

- Tobin, J. J., Hartmann, L., Chiang, H.-F., Wilner, D. J., Looney, L. W., Loinard, L., Calvet, N., & D'Alessio, P. 2013, *ApJ*, 771, 48
- Tomida, K., Tomisaka, K., Matsumoto, T., Hori, Y., Okuzumi, S., Machida, M. N., & Saigo, K. 2013, *ApJ*, 763, 6
- Tomida, K., Okuzumi, S., & Machida, M. N. 2015, *ApJ*, 801, 117
- Troland, T. H., & Crutcher R. M. 2008, *ApJ*, 680, 457
- Tsukamoto, Y., Iwasaki, K., Okuzumi, S., Machida, M. N., Inutsuka, S. 2015, *MNRAS*, 452, 278
- Tsukamoto, Y., Iwasaki, K., Okuzumi, S., Machida, M. N., Inutsuka, S. 2015, *ApJ*, 810, 26
- Umebayashi, T., & Nakano, T. 1981, *PASJ*, 33, 617
- Umebayashi, T., & Nakano, T. 1990, *MNRAS*, 243, 103
- Umebayashi, T., & Nakano, T. 2009, *ApJ*, 690, 69
- van der Tak, F.F.S., van Dishoeck, E. F. 2000, *A&A*, 358, 79
- Vrba, F. J., Coyne, G. V., & Tapia, S. 1993, *AJ*, 105, 1010
- Ward-Thompson, D., André, P., Crutcher, R., Johnstone, D., Onishi, T., & Wilson, C. 2007, *Protostars and Planets V*, p. 33
- Wardle, M., & Ng, C. 1999, *MNRAS*, 303, 239
- Wardle, M. 2007, *Ap&SS*, 311, 35
- Weingartner, J. C., & Draine, B. T. 2001, *ApJ*, 548, 296
- Williams, J. P., & Cieza, L. A. 2011, *ARA&A*, 49, 67
- Wurst, J., Price, D. J., & Bate, M. R. 2015, *arXiv:1512.01597*
- Zhao, B., Li, Z.-Y., Nakamura, F., Krasnopolsky, R., & Shang, H. 2011, *ApJ*, 742, 10
- Zhao, B., & Li, Z.-Y. 2013, *ApJ*, 763, 7
- Zhao, B., Li, Z.-Y., & Kratter, K. M. 2013, *arXiv:1308.0830*

This paper has been typeset from a  $\text{\TeX}/\text{\LaTeX}$  file prepared by the author.